1
Infrared and Raman Instrumentation for Mapping and Imaging

Peter R. Griffiths and Ellen V. Miseo

1.1
Introduction to Mapping and Imaging

The analysis of localized regions of samples by vibrational microspectroscopy can be accomplished in two ways, *mapping* or *imaging.* Mapping involves the sequential measurement of the spectrum of each adjacent region of a sample by moving each region of the sample into the beam after recording the spectrum. The measurement is repeated until the entire region of interest has been covered. Imaging, on the other hand, is like taking a digital picture and requires an image of the sample to be focused onto an array detector. The intensity of the radiation passing through each region of the sample is measured simultaneously at each pixel.

Mapping experiments in which the sample is moved in both *x* and *y* dimensions should not be properly called imaging, since the spectra have not been acquired by an array detector. However, the spectra that are obtained can be treated in exactly the same way as if these spectra had been acquired with an array detector. Commercially available hybrid mapping/imaging instruments have also been described in which a linear array of, say, 32 detectors is used to acquire a line map after which the sample is moved and the process is repeated.

In *hyperspectral imaging,* the images at more than 10 wavelength regions are recorded simultaneously with a two-dimensional array detector. Vibrational hyperspectral imaging can be accomplished through the measurement of either the mid-infrared, near-infrared (NIR), or Raman spectrum. The measurement of each type of spectrum is accomplished in different ways, although the instruments that have been developed for the measurement of NIR and Raman spectra are more closely related than that of mid-infrared hyperspectral imaging spectrometers. In NIR and Raman instruments, the signal at a given wavelength is recorded at each pixel. In NIR imaging instruments, the radiation from the source is usually focused on the sample and then passed through a monochromator or narrow bandpass filter, for example, a liquid crystal tunable filter (LCTF), before being focused on the array detector. The image from one wavelength region is measured at all pixels simultaneously. The wavelength region is then changed (usually, but not necessarily, to an adjacent spectral region) and the intensity at

each pixel is measured again. This process is repeated until all wavelengths of interest in the spectrum have been measured.

An analogous approach is used for Raman imaging, except that the monochromator must be located after the sample. The signal from all pixels for a given wavelength setting is acquired rapidly in NIR imaging instruments, where the signal-to-noise ratio (SNR) is usually high. The SNR for Raman imaging is much lower, so that a much longer integration time is needed. Thus, Raman imaging can be quite slow unless only a few wavelength regions are measured. In both NIR and Raman imaging spectrometers, the bandpass of the monochromator or filter determines the spectral resolution. Sometimes only a short spectral range or a few wavelength regions may be sufficient to classify samples that are composed of just a few components. On the other hand, for complex or previously uncharacterized samples, it is often necessary to measure data over the entire spectral range.

In mid-IR imaging instruments, it is more common to couple the array to an interferometer, so that interferograms from different spatial regions of the sample are recorded at each detector element. Subsequent Fourier transformation yields the desired hyperspectral data set. All types of systems are described in this chapter.

The end result of either spectroscopic mapping or hyperspectral imaging is an array of spectra (sometimes called a *hyperspectral cube* or *hypercube*) from which the identifying characteristics of inhomogeneous samples can be obtained. For Raman imaging, the sample does not have to be of constant thickness; however, ideally the sample should be as flat as possible. Conversely, when mid-IR or NIR transmission spectra are to be measured, the thickness of the sample should be as uniform as possible. In this case, it is sometimes possible to synthesize an image that shows the concentration of a certain component by simply plotting the absorbance at a certain wavelength of a band that is isolated from all others in the spectrum. If this approach proves to be feasible, the image may be plotted either as a gray scale, with white representing the absence of the component and dark gray representing its greatest concentration, or – more commonly – through the use of color. Many applications of imaging spectroscopy will be described throughout this book. In this chapter, the design of the instruments used to acquire these data is described.

1.2
Mid-Infrared Microspectroscopy and Mapping

1.2.1
Diffraction-Limited Microscopy

The diffraction pattern resulting from a circular aperture that is uniformly illuminated with monochromatic light has a bright region in the center, known as the *Airy disk*, which together with the series of concentric bright rings around this disk is called the *Airy pattern*. The beam half-angle θ' at which the first minimum

occurs, measured from the direction of incoming light, is given by

$$\sin \theta' = \frac{1.22\lambda}{nd} \tag{1.1}$$

where λ is the wavelength of the light and d is the diameter of the aperture. Similarly, if the half-angle of the beam at the sample is θ and n is the refractive index of the medium in which the sample is immersed, the diameter of the sample under observation, x, is given by

$$x = \frac{1.22\lambda}{n \sin \theta} \tag{1.2}$$

The product of the refractive index n and $\sin \theta$ is known as the *numerical aperture* (*NA*).

The Rayleigh criterion for barely resolving two objects is that the center of the Airy disk for the first object occurs at the first minimum of the Airy disk of the second object. Figure 1.1 shows the calculated signal from two point sources separated by 0.5λ, 1.0λ, and 1.5λ. It can be seen that the spots are not able to be distinguished when the separation is equal to 0.5λ, are just distinguishable when the separation is equal to λ, and are well separated when the spots are separated by 1.5λ.

For most transmission spectroscopic measurements made with a microscope, the sample is in contact with air and so n is usually approximately equal to 1. Since for most microscopes $\theta \sim 40°$, NA is usually close to 0.6 ($\sin 40° = 0.64$). Thus, the spatial resolution is approximately equal to λ. (We note here that the Abbe resolution is often defined as $\lambda/2$, but this performance is only accomplished for coherent illumination.) For mid-infrared measurements at the highest spatial resolution, it is customary to set the microscope aperture to give the diffraction-limited resolution at 1000 cm^{-1} ($\lambda = 10\,\mu m$) so that the resolution at longer wavelengths is set by the value at 1000 cm^{-1} (about 10 μm). Better resolution is achieved in attenuated total reflection (ATR), especially when the internal reflection element (IRE) is silicon ($n = 3.4$) or germanium ($n = 4.0$), but achieving optical spatial resolution better than about 3 μm is essentially impossible for diffraction-limited mid-infrared measurements.
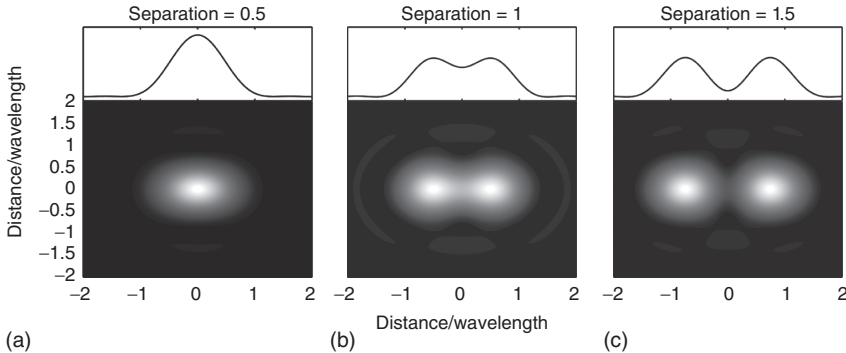

Figure 1.1 Calculated images of two point sources separated by (a) 0.5λ, (b) 1.0λ, and (c) 1.5λ. (Courtesy of Pike Technologies, Inc.)

1.2.2
Microscopes and Sampling Techniques

Although some noble efforts at fabricating a microscope for infrared spectrometry using a prism monochromator were made in the 1940s and 1950s [1–6] and PerkinElmer actually advertised a microscope that could be installed in one of their prism spectrometers [7], the performance of these early instruments was marginal and the use of infrared microscopes never caught on commercially until the late 1980s. Until that time, the mid-infrared spectra of minute samples were measured by mounting the sample behind a pinhole of the appropriate dimensions so that only the region of the sample of interest was irradiated. The sample was then held at the focus of a simple beam condenser that fit in the sample compartment of the spectrometer. As the size of the region of interest decreased, locating the sample so that the region of interest corresponded to the position of the pinhole became increasingly difficult. The situation was dramatically improved when a standard reflecting microscope was interfaced with a Fourier transform infrared (FT-IR) spectrometer. In this case, the previous function of the pinhole was replaced by a remote aperture at a conjugate focus of the sample. A simplified schematic of a typical infrared microscope is shown in Figure 1.2.

The microscope shown in Figure 1.2 is designed to operate in either the transmission mode or the reflection mode. In the transmission mode, the beam from the interferometer is passed onto a toroidal coupling optic and therefrom to the
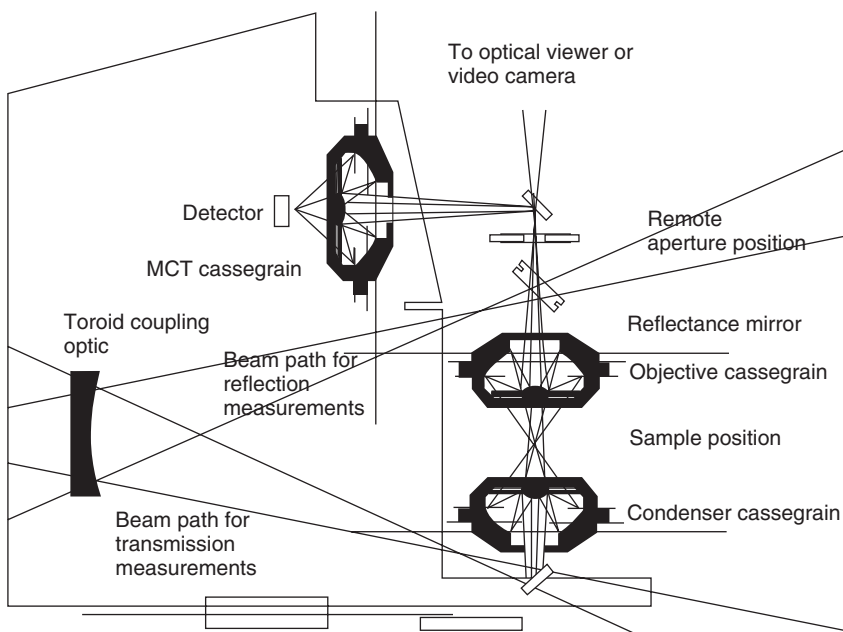

Figure 1.2 Simplified schematic of a typical microscope interfaced with an FT-IR spectrometer. (Courtesy of PerkinElmer Inc.)

Cassegrain condenser. The condenser focuses the beam into a small spot where the sample is mounted. The radiation that is transmitted through the sample is collected by a Cassegrain objective and refocused at a remote adjustable aperture. The part of beam that passes through the aperture is imaged onto an optical viewer or, more frequently today, a video camera, so that the visible image of the sample can be viewed. The sample is usually mounted on an *x, y, z* stage. The height of the sample is adjusted with the *z*-control to ensure that the position of the sample is coincident with the beam focus. The *x* and *y* controls are then used to adjust the location of the sample so that the region of interest is at the center of the beam. The jaws of the aperture are then adjusted so that only the region of interest is seen at the viewer. The aperture is often rectangular and can be rotated through 180° to allow the region of interest to be isolated. After the conditions have been optimized, a 45° mirror is slid into position so the light that is transmitted through the remote aperture is collected by the third Cassegrain and focused onto the detector, which measures the spectrum of the desired region of the sample.

We note here that the condensing mirrors go by two names: some call it a *Cassegrain* while others call it a *Schwarzschild* objective. Both objectives comprise a convex and concave mirror, with a hole in the latter for the light to travel through. The key feature of the Schwarzschild design is the concentricity, or near-concentricity, of the two mirrors; there is no requirement of concentricity whereas this is not the case for Cassegrain objectives. Thus, all Schwarzschild objectives are Cassegrain objectives but the reverse is not the case. The Schwarzschild objective has been used in almost all FT-IR microscopes, and is still used to this day as it has excellent imaging characteristics over a surprisingly wide field of view (FOV), a fact that arises from the mirror concentricity. The first commercial FT-IR microscope, the Digilab UMA-150, used this design because the designers were aware that the 1953 PerkinElmer microscope for dispersive spectrometers used such a Schwarzschild objective.

When the microscope shown in Figure 1.2 is used in the external reflection mode, the same Cassegrain is used as both a condenser and an objective. In the external reflection mode, the angle at which the toroidal coupling optic is held is switched so that the beam is passed to the top of the objective via a small deflection mirror. The size and location of this mirror are such that half the beam enters the Cassegrain. The beam is demagnified by the primary and secondary mirrors and focused on the sample, which is at the same location as for transmission measurements. The reflected beam is then reconfigured by the secondary and primary mirrors, the optical properties of which are such that the beam misses the small deflection mirror and passes to the remote aperture. Even if a perfect mirror is held at the sample focus, it can be seen that, in comparison to a transmission measurement, only half the signal can be measured when the microscope is used in its reflection mode.

Three types of external reflection spectra can be measured with the microscope optics in the reflection mode shown in Figure 1.2. In the first (which is of increasing popularity for mid-infrared spectroscopy), *transflection spectroscopy,* a sample

of thickness between 5 and 10 μm is deposited on a reflective substrate. In measurements of this type, the beam passes through the sample, is reflected from the substrate and passes back through the sample before it reemerges from the surface of the sample, and then passes to the detector. This type of measurement has occasionally been used for tissue samples and has proved quite beneficial when the sample is deposited on a "low-e glass" (low emissivity glass) slide (Kevley Technologies, Chesterland, OH), which is a glass slide that has been coated with an Ag/SnO$_2$ layer. The coating is thin enough to be transparent to visible light, but is highly reflective in the mid-infrared region. Thus, any tissue sample on these slides can be inspected by visual microscopy, and the transflection spectrum can be measured subsequently [8].

Transflection spectra have the disadvantage that radiation reflected from the front surface of the sample will also reach the detector and give rise to a distortion of the pure transflection spectrum. Merklin and Griffiths [9] showed that the contribution by front-surface reflection can be eliminated by measuring the spectrum at Brewster's angle using p-polarized radiation, that is, radiation polarized such that its electric vector is parallel to the plane of incidence. Brewster's angle for tissue samples is about 50°, which is slightly higher than the angle of incidence of most infrared microscopes, but the distortion introduced by front-surface reflection will be reduced significantly. It should be noted, however, that the use of a polarizer will reduce the SNR of the spectrum by a factor of between 2 and 3, thus this approach may not be beneficial if very small samples, such as single cells, are being investigated.

The other two types of external reflection microspectroscopy are less well suited to the characterization of tissue samples. In the first type, which is variously called *specular reflection*, *front-surface reflection*, or *Kramers–Kronig reflection*, the reflectance spectra of thick, nonscattering, bulk samples are measured and converted to the wavenumber-dependent optical constants, that is, the refractive index $n(\widetilde{\nu})$ and the absorption index $k(\widetilde{\nu})$ by the Kramers–Kronig transform, as discussed by Griffiths and de Haseth [10]. As the requirement for thick nonscattering samples is essentially never met for tissue samples, this type of measurement is never used in medical diagnosis but has occasionally been used for the study of polymer blends.

The other type of measurement that can be made with the microscope in its reflection mode is *diffuse reflection* (DR) spectroscopy. There are very few applications of mid-infrared microspectroscopy of neat samples because for mid-infrared DR spectrometry, samples should be diluted to a concentration of 0.5 – 5% with a nonabsorbing diluent, such as KBr powder, to preclude band saturation and severe distortion by reflection from the front surface of the particles. However, this mode has substantial application for NIR measurements, where sample dilution is not needed. Because absorption of NIR radiation by most samples is rather weak, they must be either at least 1 mm thick or mounted on a reflective or diffusing substrate, such as a ceramic or Teflon® disk. In the latter case, the spectrum is caused by a combination of DR, transflection, and front-surface reflection (with hopefully DR being the dominant process.)

1.2.3
Detectors for Mid-Infrared Microspectroscopy

Essentially all mid-infrared spectra are measured today by FT-IR spectrometers for which the optical path difference (opd) of the interferometers is varied rapidly and continuously. Most standard laboratory FT-IR spectrometers are equipped with a 1×1 or 2×2 mm^2 pyroelectric (either deuterated triglycine sulfate (DTGS) or deuterated L-alanine-doped triglycine sulfate (DLATGS) detector operating at or slightly below ambient temperature. However, the sensitivity of pyroelectric detectors is too low to allow them to be used to measure the relatively weak signals encountered after the beam has been passed through smaller microscope apertures than that of 100 μm. Instead, the more sensitive liquid nitrogen-cooled mercury cadmium telluride (MCT) detector is usually used. For standard FT-IR spectrometers, these detectors operate in the photoconductive (PC) mode, that is, when infrared radiation is incident on them, photons promote electrons from the valence band to the conduction band and the increase in conductivity is a measure of the photon flux.

The properties of MCT detectors depend on their composition, that is, their Hg : Cd ratio. "Narrow-band" MCT detectors are typically about 50 times more sensitive than DTGS but do not respond to radiation below ~750 cm^{-1}. The cutoff can be extended to lower wavenumber but at the expense of sensitivity. Thus, "mid-band" MCT detectors have a cutoff of about 600 cm^{-1}, but their sensitivity is about half that of the narrow-band detector. "Wide-band" detectors cut off at ~450 cm^{-1} but are even less sensitive. Fortunately, few spectra of organic samples contain useful bands much below 700 cm^{-1}, so FT-IR microscopes are almost invariably equipped with narrow-band MCT detectors. It should be noted that the response of narrow-band MCT detectors is nonlinear with radiation flux so that when large spatial regions are to be examined, the effect of this nonlinearity may become evident as a baseline offset [11].

The *noise equivalent power* (*NEP*) of an infrared detector is a measure of the noise generated by the detector and is given by

$$\text{NEP} = \frac{\sqrt{A_D}}{D^*} \tag{1.3}$$

where A_D is the area of the detector element and D^* is the specific detectivity of the detector (which is typically a constant for a given wavelength, detector composition, and temperature). The greater the NEP, the lower is the sensitivity of the detector. Most detectors are specified in terms of their D^* rather than their NEP. The D^* of a narrow-band MCT detector is close to the value given by the background limit for infrared photons and can only be improved significantly by operating at lower temperature.

From Equation 1.1, it can be seen that the area of any detector used for infrared microspectroscopy should be as small as possible. Provided that all the radiation that passes through the sample is focused on the detector, the use of a 0.25 mm detector gives an SNR that is four times greater than if a

1 mm detector were to be used for the characterization of microsamples. For mid-infrared microspectroscopy, the detector is usually a narrow-band MCT PC detector of $250\,\mu m \times 250\,\mu m$ size, although some vendors do provide options for $100\,\mu m \times 100\,\mu m$ or even $50\,\mu m \times 50\,\mu m$ sized elements. Since identical objectives are usually used to focus the beam onto the sample and the detector (see, e.g., Figure 1.1), there is 1× magnification and the *largest* sample that can be measured with a 250 μm detector is $250\,\mu m \times 250\,\mu m$; however, this is rarely a significant limitation in mid-infrared microspectroscopy when samples *smaller* than 250 μm are usually of interest.

The SNR of an FT-IR spectrum (i.e., the reciprocal of the noise of a 100% line measured in transmittance) is given by the following equation [12]:

$$\text{SNR} = \frac{U_\nu(T)\Theta\Delta\tilde{\nu}D^*t^{-\frac{1}{2}}\xi}{A_D^{\frac{1}{2}}} \tag{1.4}$$

where $U_\nu(T)$ is the spectral energy density of the source radiation ($W\,sr^{-1}\,cm^2\,cm^{-1}$), Θ is the optical throughput or *étendue* ($cm^2\,sr$), $\Delta\tilde{\nu}$ is the resolution at which the spectrum is measured (cm^{-1}), t is the measurement time (s), D^* is the specific detectivity of the detector ($cm\,Hz^{1/2}\,W^{-1}$), ξ is the efficiency of the optics, and A_D is the detector area (cm^2). Microscopes are designed to have high optical efficiency ξ and a large solid angle at the objective. The spectral resolution $\Delta\tilde{\nu}$ is determined by the nature of the sample and the information required by the operator. It is always true that the noise level is lower when the spectrum is measured at low resolution but useful spectroscopic information may be lost if the spectrum comprises narrow bands. If the spectrum comprises relatively broad bands, however, there is no point in measuring the spectrum at high resolution.

Mapping performed with a spatial resolution close to the diffraction limit can be very time consuming. For spectra measured when using sample apertures approaching the diffraction limit ($<10\,\mu m$), even a 30 s collection may result in a spectrum with a rather poor SNR and may need an increased signal averaging. It may be noted that if the measurement of each spectrum takes 30 s and a 64×64 map is required at 10 μm spatial resolution, it would take over 34 h to acquire all the spectra required for the image!

At this point, it may be asked if certain parameters can be changed to decrease the measurement time to allow maps to be acquired in reasonable times. Since the size of the remote aperture for most applications is smaller than 250 μm, it is valid to suggest that even smaller detectors should be installed in FT-IR microscopes so that the SNR is optimized for samples that are 50 μm or smaller in dimension. The answer is a very practical one: it is simply very difficult to keep the beam aligned with the tighter tolerance required for the beam to be focused accurately on a detector that is smaller than 250 μm. As described later, the situation is different when array detectors with very small pixels are used for hyperspectral imaging.

The measurement time t is largely determined by the goal of the experiment. If only a few regions of the sample are of interest, several minutes can be used for each measurement. If the sample is to be mapped, however, hundreds of spectra

are often needed and the time for each should be significantly less than a minute if the measurement is to be completed in a reasonable time.

1.2.4
Sources for Mid-Infrared Microspectroscopy

One parameter in Equation 1.2 has not yet been discussed, namely the spectral energy density, $U_\nu(T)$. The only parameter that can lead to a significantly improved SNR is the spectral energy density of the source radiation, $U_\nu(T)$. In general, the operators of laboratory FT-IR spectrometers have little control over the source installed in their instruments. Most instruments are equipped with an incandescent silicon carbide source, such as a Globar®, operating at about 1400 K. The emission characteristics of mid-infrared sources are usually similar to those of a blackbody, so that it is possible to increase the spectral energy density with an increase in the temperature of the source. However, increasing the temperature of a Globar often leads to cracking and the rapid degradation of the electrical contacts at the end of the rod. One material that has been reported to be operable to over 1950 K is molybdenum silicide. Another source that can be taken up to a temperature close to 2000 K is a homogeneous material with the chemical formula $Mo_x W_{1-x} Si_2$, which is commercially available under the name Kanthal Super 1900. The molybdenum and tungsten atoms are isomorphous in this chemical formula, and can thus replace each other in the same structure. However, a detailed comparison of any of these materials with a Globar with respect to infrared microspectroscopy has never been reported to the best knowledge of these authors.

Provided that samples can be removed from the laboratory, there are two alternative sources of infrared radiation that are far better than incandescent sources for mid-infrared microspectroscopy, namely the *synchrotron* and the *free electron laser* (FEL) [13]. A synchrotron is a particular type of cyclic particle accelerator, or cyclotron, in which the particles are electrons. A magnetic field is used to bend the path of the electrons, and an electric field is used to accelerate them. Both fields are carefully synchronized with the traveling beam of electrons. By increasing the two fields appropriately as the particles gain energy, their path can be controlled as they are accelerated. This allows the particles to be contained within a large narrow ring with some straight sections between the bending magnets and some bent sections within the magnets giving the ring the shape of a round-cornered polygon. This shape also allows (and, in fact, requires) the use of multiple magnets to bend the particle beam. The strength of the transverse magnetic field is varied periodically by arranging magnets with alternating poles along the beam path. This array of magnets is sometimes called an *undulator*, or *wiggler*, because it forces the electrons in the beam to assume a sinusoidal path. The acceleration of the electrons along this path results in the release of a photon.

In a typical cyclotron, the maximum radius is quite limited as the particles start at the center and spiral outward; thus, the entire path must be a self-supporting disk-shaped evacuated chamber. Since the radius is limited, the power of the

device becomes limited by the strength of the magnetic field. Synchrotrons overcome this limitation through the use of a narrow beam pipe that can be surrounded by much smaller and more tightly focused magnets. The ability of this device to accelerate particles is limited by the fact that the particles must be charged to be accelerated at all, but all charged particles under acceleration emit photons, thereby losing energy. The limiting beam energy is reached when the energy lost to the lateral acceleration required to maintain the beam path in a circle equals the energy added to each cycle. More powerful accelerators are built using larger radius paths and more numerous, powerful cavities to accelerate the particle beam between corners. Recent advances in the instrumentation for mid-infrared microspectroscopy using a synchrotron source are discussed in more detail in Chapter 15.

An FEL shares the same optical property as a conventional laser, that is, the emission of a beam of coherent electromagnetic radiation that can reach high power. However, FELs use some very different operating principles than a conventional laser to form the beam. Unlike conventional lasers that rely on bound atomic or molecular states, FELs use a relativistic electron beam as the lasing medium, which gives them the widest frequency range of any laser type, and make many of them widely tunable, currently ranging in wavelength from microwaves to soft X-rays. In certain respects, the FEL is similar to a synchrotron. To create an FEL, a beam of electrons is accelerated to relativistic speeds. As in the operation of a synchrotron, the beam passes through a periodic, transverse magnetic field. However, in an FEL, the undulator is placed in an optical cavity or a resonator that reflects the emitted light back and forth. The electrons become tightly bunched because of interactions with a light beam that is also passing through the undulator. The light either may be introduced from an external "seed" laser or, more frequently, is the radiation that has been generated from a previous bunch of electrons that is reflected from mirrors that form an optical cavity outside the undulator.

Viewed relativistically in the rest frame of the electron, the magnetic field can be treated as if it were a virtual photon. The collision of the electron with this virtual photon creates an actual photon by Compton scattering. Mirrors capture the released photons to generate a resonant gain. The wavelength can be tuned over a wide range by adjusting either the energy of the electrons or the field strength. Since the energy of the emitted photons is governed by the speed of the electron beam and magnetic field strength, an FEL can be tuned. Furthermore, because the resonance is specific for light of a given wavelength, the power of the beam is significantly greater than that of a synchrotron, for which broadband radiation is emitted.

What makes this device a laser is that the electron motion is in phase with the field of the light already emitted, so that the fields add coherently. As the intensity of the emitted light depends on the square of the field, the light output is increased. In the rest frame moving along the undulator, any radiation will still move with the speed of light and pass over the electrons, allowing their motion to become synchronized. The phase of the emitted light is introduced from the outside. Depending on the position along the undulator, the oscillation of the

electrons is in-phase or out-of-phase with the radiation introduced from the outside. The light tries to either accelerate or decelerate these electrons. It thereby gains or loses kinetic energy, so it moves faster or slower along the undulator. This oscillatory motion causes the electrons to form bunches. When the photons are synchronized with the field, coherent radiation is emitted.

Steiner *et al.* [14] have reported the measurement of maps of octadecanephosphonic acid (OPA) molecules deposited on a microstructured aluminum oxide/gold surface using an FEL source that was modulated by a rapid-scanning interferometer. The beam was then passed through a wire-grid polarizer and a photoelastic modulator so that the polarization was switched at a rate of 75 kHz. The beam was then passed through a pinhole and focused onto the sample with a Cassegrain objective at an incidence angle of about 60° such that the diameter of the Airy disk was about 15 μm. Light that was polarized such that the electric vector was parallel to the surface was absorbed by the surface species, whereas light that was polarized such that the electric vector was perpendicular to the surface was not absorbed. The beam was collected by a second Cassegrain and then refocused at the detector. As the detector signal is passed into a lock-in amplifier referenced to the polarization modulation frequency, the interferogram was caused only by the surface species [15]. The sample was moved in a raster fashion in order to generate the map. The spectroscopic map revealed that OPA is attached on the aluminum oxide surface and not to gold. The attached molecules form a highly ordered film. A lower degree of ordering was found for phosphonic acid adsorbed on gold. Under normal conditions, the operators of the FEL need 10 – 20 min to change the wavelength of the FEL. Thus, it required at least a day to measure the image at just three wavelengths.

From a spectroscopic standpoint, the main difference between a synchrotron and an FEL is that a synchrotron emits broadband radiation while the FEL emits monochromatic radiation with several orders of magnitude of higher brilliance than a synchrotron. Thus, radiation from a synchrotron can be expanded and passed into an FT-IR spectrometer, for which the interferometer and all the subsequent optics are no different from those in a conventional FT-IR spectrometer (or microspectrometer). When an FEL is used for spectroscopy, the monochromatic radiation that is generated can be modulated in any appropriate manner (e.g., by a tuning fork chopper) before being passed onto the sample and detector. In principle, FELs can be used for imaging by passing monochromatic radiation onto a focal-plane array (FPA) detector and measuring the signal from each pixel (see below), although such experiments have not yet be reported. The laser would then be tuned to the next wavelength of interest, and this process would be repeated for as many wavelengths as are needed to characterize the sample.

The synchrotron has an equivalent blackbody temperature of 10 000 K [16]. The effective diameter of the beam from a synchrotron is typically about 100 μm and light is emitted into a narrow range of angles, making this an almost perfect radiation source for mid-infrared microspectroscopy. Not all synchtrotrons are equipped with infrared beam lines, but as the importance of the results that are being obtained continues to increase, this situation is changing. Beam time on

most synchrotrons is highly prized and potential users often have to write a short proposal to be granted beam time. However, since FT-IR microscopes with a synchrotron source allow spectra with diffraction-limited spatial resolution and high SNR to be measured in a few seconds, many spectroscopists are starting to use the combination of synchrotron source, FT-IR spectrometer, and either a single-element detector or an array detector [17–20].

1.2.5
Spatial Resolution

Today, FT-IR microscopes are designed to allow spectra of physically small samples, or regions of small samples, to be measured as quickly and easily as possible. On most microscopes, a video image of the sample is displayed on the monitor screen immediately adjacent to the sample, allowing the position of the sample and the jaws of the aperture to be optimized prior to the measurement of the spectrum. A motorized sample stage allows mapping to be readily accomplished.

As noted above, the best spatial resolution of a microscope is ultimately determined by diffraction of the radiation. Thus, the spatial resolution is limited by the radius r of the Airy disk for the longest wavelength in the spectrum and hence depends on n, the refractive index of the medium in which the optics are immersed, for example, 1.0 for air and up to 1.56 for oils. Oil immersion is almost never used for infrared microspectroscopy because of absorption by the oil but has occasionally been used to improve the spatial resolution in Raman microspectroscopy. Immersion oils have been shown to be essential in order to obtain good depth resolution with confocal Raman microscopy [21]. Of greater importance from a practical standpoint for infrared microspectroscopy is the improvement in spatial resolution that is achieved in an attenuated total reflection (ATR) measurement with a hemispherical IRE, especially when the IRE is fabricated from germanium ($n = 4.0$) or silicon ($n = 3.4$.)

Although it was stated that the spatial resolution of a microscope is ultimately limited by diffraction, all modes of chemical imaging employ detector elements of finite size. When the image of the detector element (or pixel for measurements made with an array detector, see below) at the sample plane becomes the limiting aperture, it can often become the limiting factor determining the ultimate spatial resolution before wavelength-limited diffraction effects become apparent. As the wavelengths of radiation across the mid-infrared spectrum typically range from 2.5 to about 14 µm, if the pixel size at the sample plane (which is a function of native detector pixel size and overall system magnification) is larger than the wavelength being used to measure it, then the system is said to be "pixel-size limited." Conversely, if the wavelength of light being used to measure the sample is smaller than the pixel size at the sample plane, the system is said to be "diffraction limited." This is an important, yet often misunderstood, concept. For example, the use of higher magnification objectives, such as 36×, results in very small images at the sample plane. However, this does not necessarily result in improved spatial resolution,

as these systems are often already diffraction limited. For some imaging systems that incorporate FPA detectors, a pixel size of 1.1 µm has been reported when a 36× objective is used, but this is a "waste of pixels" as the pixel size is significantly smaller than the wavelengths of light in the mid-infrared, that is, the resolution is already diffraction limited. In the example of the 36× objective providing a 1.1 µm pixel size, this spatial resolution could only really be achieved at 9000 cm^{-1}, well beyond the high wavenumber cutoff of the FPA.

Several types of microscopes are commercially available for mid-infrared microspectroscopy; they differ in how the sample is apertured and how the light is transferred within the microscope. The first has the simple design concept shown in Figure 1.2, such that the beam from the interferometer is focused at the sample; thus, the sample is at an image of either the source or the Jacquinot stop (for higher resolution FT-IR spectrometers). The beam is then refocused at the remote aperture and then again onto the detector. In the alternative design, the beam from the interferometer is passed through two apertures, one before and one after the sample, as shown schematically in Figure 1.3. This approach, which was originally called *redundant aperturing* and is now more frequently known as *dual aperturing*, gives slightly higher spatial resolution near the diffraction limit than the single-aperture design, as shown theoretically in Figure 1.4. The second aperture serves much the same purpose as the pinhole in a confocal microscope
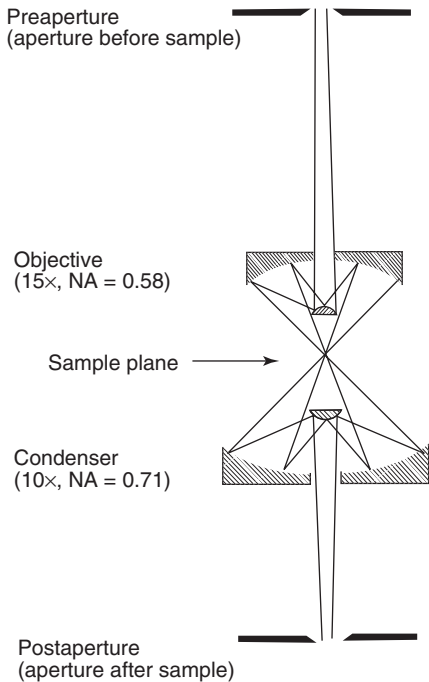
Preaperture
(aperture before sample)

Objective
(15×, NA = 0.58)

Sample plane ⟶

Condenser
(10×, NA = 0.71)

Postaperture
(aperture after sample)

Figure 1.3   Dual-aperture microscope similar to the optics of an IRPlan microscope. (Reproduced with permission from Ref. [22]. Copyright 1991, Society for Applied Spectroscopy.)
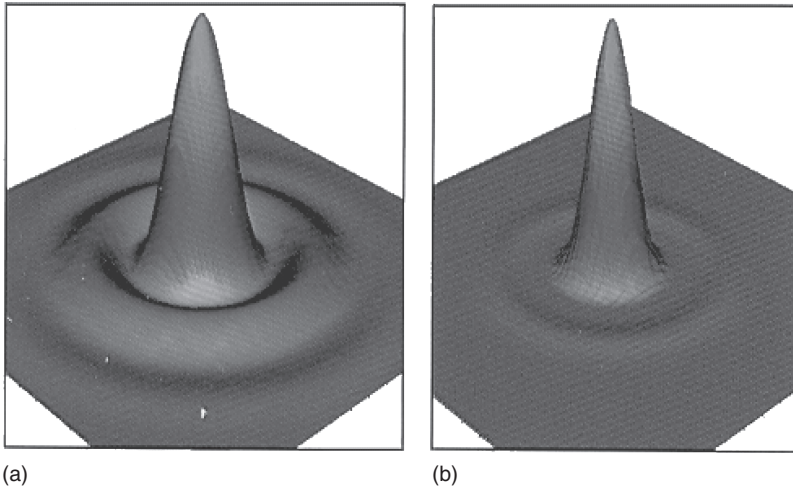
(a)   (b)

Figure 1.4 (a) Energy profile showing the diffracted radiation outside the area defined by a single aperture. (b) Corresponding profile obtained with masks located before and after the sample. (Reproduced from Ref. [10]. Copyright 2007, John Wiley & Sons.)

(see below). The performance for dual remote apertures and a single aperture located before the sample is comparable, as shown in Figure 1.4. However, it should be noted that the dual-aperture design has the limitation that less energy reaches the detector than with the single-aperture design, so that the SNR for a given spatial resolution is decreased (Figure 1.5).
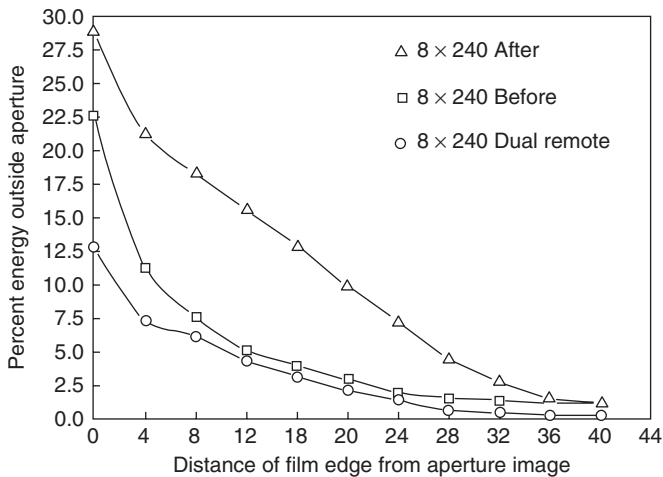

Figure 1.5 Percent of stray energy outside the area defined by an $8\,\mu m \times 240\,\mu m$ rectangular aperture for various imaging modes. (Reproduced with permission from Ref. [22]. Copyright 1991, Society for Applied Spectroscopy.)
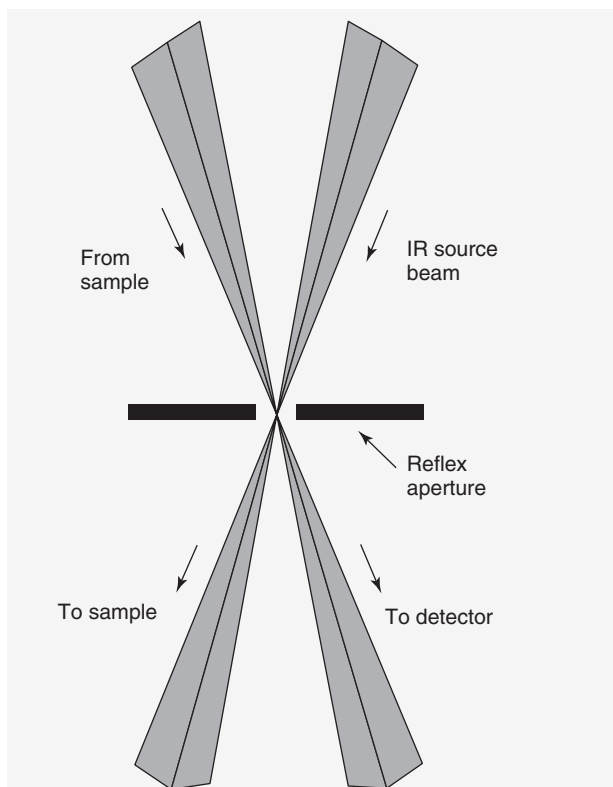
Figure 1.6 Dual confocal aperturing achieved with a single physical aperture. (Reproduced from Ref. [10]. Copyright 2007, John Wiley & Sons.)

It was found that keeping the apertures of a dual-aperture microscope in alignment over a long period of use was not an easy task, especially when high spatial resolution is desired and the apertures must be very small. Thermo-Fisher devised a clever scheme to get around the latter problem by using the same aperture twice, in the way shown in Figure 1.6.[1] The dual-aperture concept is similar to that of a confocal microscope (see below, Section 1.3.1). Both the dual-aperture design and confocal microscopes preclude imaging measurements; however, in order to image a sample, all regions of the sample that are of interest must be completely illuminated by the source radiation and the detector pixels serve the purpose of the remote aperture that would normally be located after the sample. The dual-aperture system is ideally suited to mapping measurements with diffraction-limited spatial resolution, in

1) Nicolet Corporation made its first FT-IR spectrometer in 1971 and became the market leader shortly afterwards. In 1995, Thermo Electron Corporation purchased Nicolet. In 2006, Thermo Electron purchased Fisher Scientific and the corporation is now known as *Thermo-Fisher*.

which case a source of very high brightness such as a synchrotron would be beneficial.

Transmission Microspectroscopy

Occasionally, transmission spectra of small inhomogeneous samples show the presence of artifacts. For example, the effect of scattering may cause symmetrical bands to lose their symmetry. Instead of having the symmetric shape of the absorption index spectrum, the stronger bands start to take on appearance of the refractive index spectrum. (This phenomenon is sometimes called the *Christiansen effect* [23].) Romeo *et al.* [24, 25] observed a second effect caused by light scattering while measuring the infrared spectrum of whole cells by FT-IR microspectroscopy. They demonstrated that light scattering by the nucleus introduces a broad undulating spectral feature into the baseline of the spectrum, which they attributed to Mie-type scattering by the cell nucleus. Dielectric spheres are known to scatter electromagnetic radiation if the wavelength of the light is comparable to the size of the dielectric sphere. The theory of this scattering process was first described theoretically by Mie [26] and has been nicely summarized by Romeo *et al.* [24, 25].

Davis *et al.* [27–29] have recently published a comprehensive framework for the infrared microscopic analysis of both homogeneous and heterogeneous materials. This framework validated by experimental data can be used to explain distortions in microspectroscopic data and, as shown in the cited work, to recover the spectra. Mie theory assumes a spherical scattering particle in the field of a plane electromagnetic wave. The scattering cross section Q_{sca} of a dielectric sphere interacting with a plane electromagnetic wave is given by a series expansion of the size parameter ρ and complicated expressions in the half-integer order Bessel (Ricatti–Bessel) functions of the first kind and their complex equivalents (Hankel functions). The size parameter ρ is defined by

$$\rho = \frac{2\pi r m_o}{\lambda} \tag{1.5}$$

where r is the radius of the sphere, λ the wavelength of the light, and m_o the ratio of refractive indices between the sphere and the surroundings. The Bessel functions account for the undulating wavelength dependence of Mie scattering.

The angular dependence of Mie scattering is given by series expansions in the Legendre polynomials and their derivatives with respect to the scattering angle. Although the exact solution of this problem is rather complex, Diem's group also used an approximate formula, which was first reported by Walstra [30]:

$$Q_{sca} = 2 - \left(\frac{4}{\rho}\right)\sin\rho + \left(\frac{4}{\rho^2}\right)(1 - \cos\rho) \tag{1.6}$$

where ρ is the size factor defined earlier. This approximation reproduces the rigorous calculation within 1% and matches the spectra remarkably well. Using the approximate calculations, Romeo *et al.* were able to model the Mie scattering

background satisfactorily and correct the distorted spectra by subtracting the modeled Mie background.

1.2.7
Attenuated Total Reflection Microspectroscopy

It can be seen from Equations 1.3 and 1.4 that the spatial resolution of infrared microspectroscopy can be improved by immersing the sample in a medium of high refractive index. This is exactly what is done in ATR spectroscopy using a single-reflection hemispherical IRE. For example, if a germanium ($n = 4.0$) hemispherical IRE is used, not only do you get an increase in the NA because of the increased refractive index of Ge, but also the outer ray angle of incidence (which defines NA) is increased, as the light is refracted inward. The difference between the focusing that occurs with a triangular prism and a hemispherical IRE is seen in Figure 1.7a,b.

The first ATR accessory to make use of a single-reflection IRE with approximately hemispherical geometry was the Split Pea (Harrick Scientific), the usual image size of which is about 250 µm when used with a germanium IRE. Although germanium has the highest refractive index of infrared transparent materials (and therefore gives the greatest demagnification), it has the great disadvantage that it is opaque to visible light. As a result, sample alignment in some of the earlier devices was quite tricky. Since the introduction of the Split Pea, a number of analogous accessories have been introduced for ATR microspectroscopy, including several that have been explicitly designed to replace the objective in a standard infrared microscope. The Bruker Optics Hyperion, the optics of which are shown in Figure 1.8, is just one example of a microscope designed for FT-IR microspectroscopy and analogous systems are available from a number of different vendors. Several manufacturers have designed accessories where
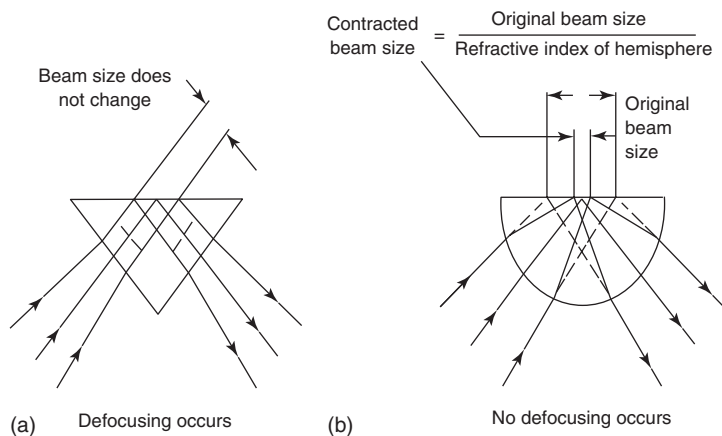

$$\text{Contracted beam size} = \frac{\text{Original beam size}}{\text{Refractive index of hemisphere}}$$

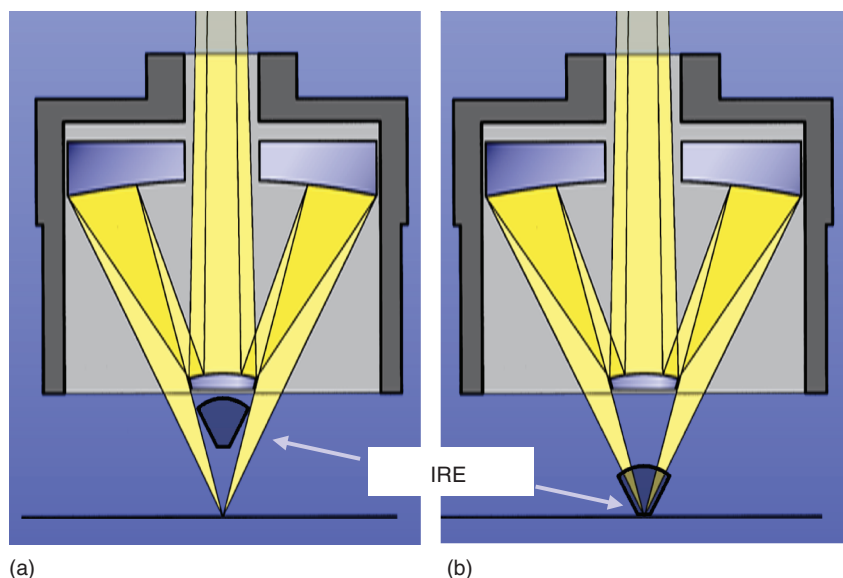**Figure 1.7**   Beam focusing through (a) prismatic and (b) hemispherical internal reflection element.

Figure 1.8 Optical schematic of the Bruker Optics ATR objective used in the (a) alignment mode and (b) spectral acquisition mode. (Courtesy of Bruker Optics.)

the sample can be aligned without being in contact with the IRE. Once the appropriate region has been selected, the IRE is moved into place. With the Bruker Hyperion, the tip of the IRE is 100 μm in linear dimension to achieve high spatial resolution. It is equipped with an electronic pressure sensor to ensure good contact with the sample, which is particularly important for mapping by ATR microscopy. The IRE is spring loaded to avoid damage, and there are five different pressure steps to allow optimal contact for hard and soft samples.

Similar to germanium, silicon also has a fairly high refractive index ($n = 3.4$). Silicon is rarely used for the fabrication of large IREs, for which the optical path may be several centimeters, because the presence of trace impurities leads to excessive absorption of the radiation below about 1200 cm^{-1}. With the very short path through the IRE installed in a microscope objective, however, this is no longer a problem. Thus, either silicon or germanium can be used productively as the IRE in an ATR objective.

1.3
Raman Microspectroscopy and Mapping

1.3.1
Introduction to Raman Microspectroscopy

In principle, Raman microspectroscopy is attractive because the practical diffraction limit is on the order of the excitation wavelength, which is about 10×

smaller for Raman spectroscopy with a visible laser than that for mid-infrared spectroscopy. It is therefore possible to focus visible or NIR laser light to much smaller spot sizes (~1 μm or less) than that may be examined by mid-infrared radiation. Until the mid-1980s, however, Raman spectrometry was a relatively unpopular, time-consuming technique for the characterization of both macro- and microsamples for the following reasons:

- The intensities of strong bands in Raman spectra are usually at least 10^8 times weaker than the intensity of the incident monochromatic beam.
- When photomultiplier tubes (PMTs) were used for the detection of Raman spectra, high-power gas lasers, such as Ar^+, were required to yield enough photons for the measurement of Raman spectra in less than 1 h; the power supplies for the early versions of these lasers generated so much heat that they often required water cooling.
- Inefficient double, and occasionally triple, monochromators were required to eliminate stray light from the Rayleigh line.
- No multiplex or multichannel technique was available for the measurement of Raman spectra, so instruments were based on scanning monochromators with a single PMT detector.
- Many "real-world" samples fluoresce when illuminated with visible light, especially green light from a frequency-doubled neodymium-doped yttrium aluminum garnet (Nd:YAG) laser at 532 nm or from an argon ion laser at 488 or 514.5 nm.

Even though nothing can be done to make the Raman cross section of vibrational bands any greater without the application of such techniques as resonance Raman spectroscopy or surface-enhanced Raman scattering (SERS), several important technological developments led to the design of today's truly powerful Raman spectrometers. These included (in no particular historical order) the development of the following:

- highly efficient notch filters that eliminate the Rayleigh line and transmit both the Stokes- and anti-Stokes Raman bands or edge filters that transmit only the Stokes Raman bands and block all shorter wavelength radiation, eliminating the need for the second or third monochromator;
- small, efficient single monochromators based on concave holographic gratings, transmission holographic gratings, or standard Czerny–Turner monochromators in combination with a notch filter;
- "scientific" charge-coupled device (CCD) array detectors with quantum efficiencies close to 100% and, more recently, electron-multiplied CCDs (see Section 1.3.2);
- diode lasers emitting at 785 and 840 nm, which minimize fluorescence and are still compatible with silicon-based CCD detectors over much of the Raman spectrum;
- diode-pumped Nd:YAG lasers emitting at 1064 nm: with a laser operating at this long wavelength, fluorescence from the sample is often minimized and sometimes eliminated;

- the frequency-doubled Nd:YAG laser emitting at 532 nm that requires far less power than an Ar^+ laser;
- efficient fiber-optic probes.

Fourier transform (FT) Raman spectrometry, which was needed because the Raman spectrum generated 1064 nm radiation, is at too long wavelength for polychromators equipped with silicon-based CCD detectors. The first report of the design and testing of an FT-Raman spectrometer was by Hirschfeld and Chase in 1986 [31], and these instruments became commercially available the following year. NIR laser excitation is needed because many compounds fluoresce when illuminated with visible light leading to excess photon shot noise. With most FT-Raman spectrometers, the sample is illuminated with a 1064 nm radiation from a Nd:YAG laser, and the Rayleigh and Raman-scattered light is modulated by a two-beam interferometer. After removal of the Rayleigh-scattered radiation by a notch or edge filter, the Raman interferogram is detected with either an indium gallium arsenide (InGaAs) or germanium detector. Within another year, however, multichannel Raman spectrometers based on a polychromator and a CCD array detector were also brought onto the market. These instruments were compatible with essentially any laser that led to the generation of a Raman spectrum at shorter wavelength than the 1100 nm cutoff of silicon-based CCD detectors. CCD-Raman spectrometers with longer wavelength lasers and InGaAs array detectors are commercially available, but these instruments rarely have the sensitivity to be used in conjunction with a microscope.

The development of CCD-Raman spectrometers revolutionized Raman spectroscopy. Within the space of about 5 years, about 10 Raman spectrometers based on multichannel technologies were introduced commercially. Several of the CCD-Raman spectrometers were either designed for or could be readily modified for microspectroscopy. Although FT-Raman microspectrometers have been reported (e.g., [22]), they have not proved very popular for three reasons: safety, sample heating, and sensitivity. In practice, therefore, CCD-Raman spectrometers have proved to be far more successful for Raman microspectroscopy than FT-Raman spectrometers and most instruments are based on this concept.

Raman microspectroscopy is not a new concept. In 1966, Delhaye and Migeon [32] showed that a laser beam could be tightly focused at a sample, and that Raman-scattered light could be collected and transferred to a spectrometer with minimal loss. Their calculations showed that the increased irradiance more than compensated for the decrease in the size of the irradiated volume. The first Raman microscope was reported by Delhaye and Dhamelincourt in 1975 [33]. An instrument based on these principles (the MOLE™) was introduced by Jobin-Yvon at about the same time; however, the optical scheme used for imaging, which employed global illumination, was inefficient and it was not until the advent of CCD-Raman spectrometers that the advantages of Raman microscopy became apparent.

Arguably the most important advantage of many microscopes used for Raman microspectroscopy is the fact that they have a confocal design. In a typical confocal design, see Figure 1.9, the laser beam is focused on a small aperture (to clean
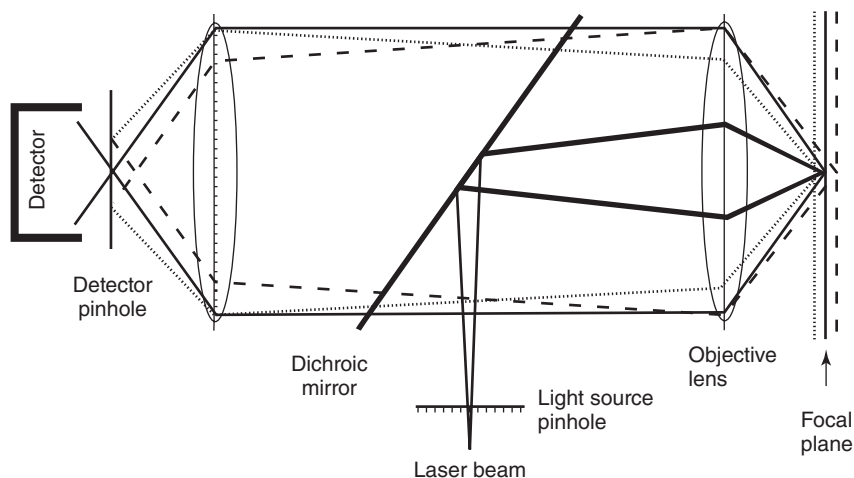
Figure 1.9 Schematic representation of the optics of a confocal microscope.

up the beam profile and present a diffraction-limited source) and then refocused by an objective lens with a large NA onto a small (ideally diffraction-limited) focal volume within the sample. A mixture of the Raman- and Rayleigh-scattered light from the illuminated spot is then collected by the objective lens. The high NA of these optics allows the light to be collected over a solid angle of almost a full hemisphere. An objective with a NA of 0.95 collects about 70% of the radiation emitted over 2π steradians. A dichroic beamsplitter (typically a notch filter or an edge filter) reflects the radiation from the Rayleigh line and transmits the Stokes-shifted Raman-scattered radiation at longer wavelength. After passing through a pinhole, the Raman-scattered light is passed into the monochromator and the intensity at each wavelength is measured. The small spot enables the image to be transferred to the spectrometer though the narrow (typically about 100 μm) entrance slit with minimal loss in energy. Today, most Raman microspectrometers employ confocal optics, which give the capability to produce blur-free images of thick samples at various depths. It may be noted, however, that spherical aberration limits sampling with diffraction-limited resolution at depths much greater than 10 μm.

As seen in Figure 1.9, the detector pinhole obstructs the so-called out-of-focus (or out-of-plane) light, especially light from adjacent spatial regions and fluorescent emission not originating from the focal plane of the objective lens. Light rays from below the focal plane come to a focus before reaching the detector pinhole, and then expand out so that most of the rays are physically blocked from reaching the detector by the pinhole. In the same way, light from above the focal plane is focused behind the detector pinhole, so that most of this light is also vignetted by the pinhole and is not detected. However, all the light from the illuminated focus (solid lines) is imaged at the pinhole and passed to the detector. The detected light originating from an illuminated volume element within the specimen is then focused on the entrance slit of a polychromator and the spectrum is measured

with a CCD detector. Since the out-of-focus rays from above and below the focal plane are largely removed, sharper images are measured than can be acquired from conventional (nonconfocal) microscopy techniques. Mapping is accomplished by moving the sample by small amounts after each spectrum has been recorded.

Several modes of operation are available in state-of-the-art confocal Raman microspectroscopy, including the measurement of samples with a spatial resolution of less than 1 μm, depth profiling, and line mapping. LaPlant and Ben-Amotz have given a detailed description of the design and construction of a confocal Raman microspectrometer [34] and a number of instruments are available commercially.

Several companies market Raman spectrometers with confocal optical configurations. The WITec alpha300 R confocal Raman microscope differs from other confocal Raman microspectrometers in that it has been designed especially for fast microspectroscopy. The data acquisition time for entire spectra can be less than 1 ms, which allows Raman mapping of over 10 000 spectra in less than a minute when the Raman signal is adequate. These data sets can already be evaluated during data acquisition by using filters. For example, the integrated intensities of certain bands of interest may be calculated or the position or full width at half maximum of the bands may be evaluated. Band fitting to Gaussian or Lorenzian shapes, as well as various other fitting algorithms, can also be applied to the data set. Using these filters, several 3D data sets that can be displayed as images are created from the 4D hyperspectral data.

The WITec alpha300 R confocal Raman microscope can be upgraded to perform atomic force microscopy, tip-enhanced Raman spectrometry, and near-field scanning optical microscopy, and is arguably the most versatile instrument for Raman microspectroscopy available today, although the competition is rapidly closing the gap.

1.3.2
CCD Detectors

The quantum efficiency of contemporary array detectors can be remarkably high – greater than 90% in the case of back-illuminated CCDs. The two main sources of noise for CCD cameras are as follows:

- dark current, which is largely caused by thermal emission and is usually reduced to a negligibly low level by thermoelectrically cooling the detector below -60 °C, and
- readout noise, which is the number of electrons introduced per pixel into the final signal upon the readout of the device and is caused by both the lack of repeatability of the conversion from an analog signal to a digital number and the introduction of spurious electrons into the camera electronics, leading to unwanted random fluctuations in the output. Readout noise, which is usually given in terms of electrons, is dependent on the readout rate; typical values are

from 5–10 electrons for a 50 kHz readout rate to ∼30 electrons for a 2.5 MHz readout rate.

The combination of these two random effects produces an uncertainty in the final output value for each pixel. In the output of the CCD image, readout noise is added into every pixel every time the array is read out. This means that a CCD with a readout noise of 30 electrons will, on average, contain 30 extra electrons of charge in each pixel upon readout. As a consequence, CCDs with high readout noise (more than 80–100 electrons) are not very good to use if a sequence of short exposure frames is co-added instead of using one long exposure. However, for modern scientific CCDs, readout noise values are very low, in the range of 10 electrons per pixel per read or less. Ideally, the limiting noise source in any Raman spectrometer should be photon shot noise. Because photons follow Poisson statistics, for a given signal the uncertainty is the square root of the signals in electrons. In this case, the SNR of many Raman spectra can be remarkably high, even though the signal is so low. For example, even if only 100 photons are detected (converted to electrons), the SNR is still 10 provided that the only noise source is photon shot noise.

For Raman mapping measurements, the readout time per pixel must be very short. For example, if an image consisting of 128 pixels/line and 128 lines is acquired with an integration time of 1 s/pixel, the total acquisition time is just a little over 4.5 h. Reducing the readout time to 100 ms/pixel decreases the measurement time to 27 min. A further 10-fold increase in the readout rate decreases the acquisition time to less than 3 min. The latter situation would allow hundreds of images to be acquired per day instead of just one or two. Unfortunately, this condition is not readily achievable in practice because the faster is the readout time of the detector electronics, the noisier is the readout amplifier.

Hollricher and Ibach [35] have described how the SNR of Raman spectra can be increased through the use of an electron multiplying charge-coupled device (EMCCD). This device is a normal CCD with an additional readout register that is driven with a significantly higher clock voltage than a normal CCD readout register. The effect of the high clock voltage is to affect an electron multiplication through impact ionization. In practice, the gain may be increased by a factor of up to 1000 in this way, so that the photon shot noise is always much greater than the readout noise. The SNR of Raman bands does not increase linearly with the gain and is actually reduced at high gain; typically the optimal SNR achieved through the use of an EMCCD is about five times greater than if the same spectrum had been measured with a conventional CCD array. The improved SNR allows superb images to be obtained from Raman mapping experiments in a remarkably short time. For example, a 200×200 pixel color-coded image of a 7.1 nm layer of poly(methyl methacrylate) (PMMA) contaminated with 4.2 nm fibers acquired with a WITec alpha300 R confocal Raman microscope is shown in Figure 1.10. The integration time was 7 ms per spectrum for a total acquisition time of less than 6 min.
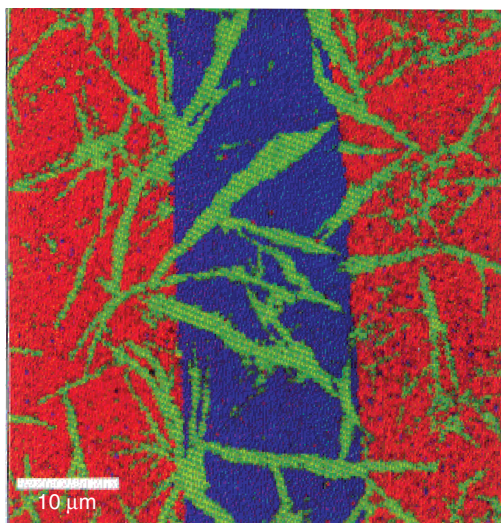
Figure 1.10 Color-coded confocal Raman map of a 7.1 nm thick PMMA layer (red) and a 4.2 nm contaminant layer (green) on glass (blue). The map was computed from 200×200 spectra, with an integration time of 7 ms per spectrum, for a total acquisition time of 5.4 min. (Reproduced with permission from Ref. [35] Spectroscopy Supplement, June, 2007. Copyright 2007, Avanstar Publications.)

Another source of "noise" in spectra measured using a CCD is caused by the pixel-to-pixel variation in the quantum efficiency of neighboring pixels. This variation can be corrected by illuminating the detector array with a uniform light source and measuring the signal from each pixel. Once the relative response of each pixel has been determined, a correction known as a *flat field correction* can be applied.

Despite all the efforts to minimize the noise in Raman spectra measured in the short times needed for mapping measurements, it is rare that the spectroscopist would not be more satisfied if the SNR were higher. Cai *et al.* [36] reported a more powerful way of reducing the noise in Raman spectra with less band broadening than Savitzky–Golay [37] smoothing. In their approach, multiresolution wavelet transformation and block thresholding were used to both suppress the background caused by fluorescence and reduce the noise without a significant loss in spectral resolution.

1.3.3
Spatial Resolution

For diffraction-limited microscopy, it may be thought that the image should be focused on the CCD such that the Airy disk fills one pixel. However, Adar *et al.* [38] demonstrated that image quality can be improved significantly if the sample step is much smaller than the spatial resolution of the measurement. For example,
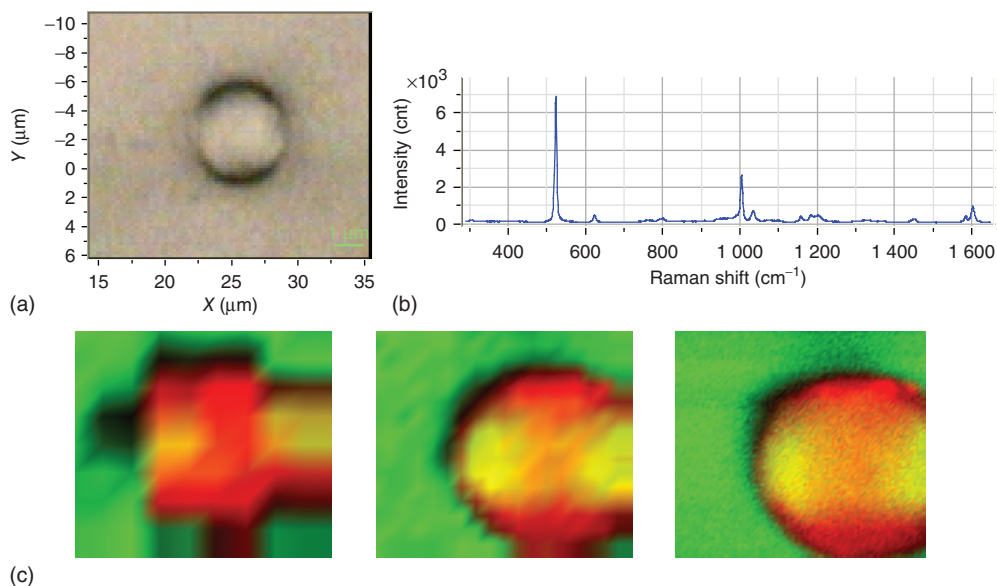
(a)

(b)

(c)

Figure 1.11 (a) Visual image of a 1 μm diameter polystyrene bead. (c) Raman image of this bead, recorded with a 100× (NA = 0.95) infinity-corrected microscope objective at increments of 1.0, 0.5, and 0.1 μm/step. (b) Raman spectrum measured from the center of one of these beads. (Reproduced with permission from Ref. [38]. Copyright 2006, Avanstar Publications.)

Figure 1.11 shows the Raman map of an 8 μm polystyrene bead on a silicon substrate recorded with a 100× objective with steps of 1.0, 0.5, and 0.1 μm. The visual image recorded through a standard optical microscope is shown for comparison. Clearly, reconstructing the image from data taken with steps smaller than the resolution given by the Rayleigh criterion gives a higher quality Raman image.

The strength of the objective is also important, as it controls the NA. Figure 1.12A shows Raman maps of five 5.18 μm polystyrene spheres recorded with 100×, 50×, and 20× objectives, with the increment between data points being 0.2 μm and Figure 1.12B shows the line profiles across the two beads at the top right of these images.

Information can also be collected from different focal planes by raising or lowering the microscope stage. The computer can generate a 3D picture of a specimen by assembling a stack of these 2D images from successive focal planes. Some care is needed in the interpretation of the results obtained by depth profiling with a confocal Raman microscope, however. For example, Everall [39] has shown that when using metallurgical objectives, which are typically supplied as standard with confocal Raman microscopes, the focus is both much deeper than might be first thought and blurred because of spherical aberration, as shown in Figure 1.13. Even in the absence of spherical aberration, Everall showed that bands originating from sample regions far above and below the optimum focal plane can still contribute significantly to the spectrum [40]. He demonstrated this by investigating
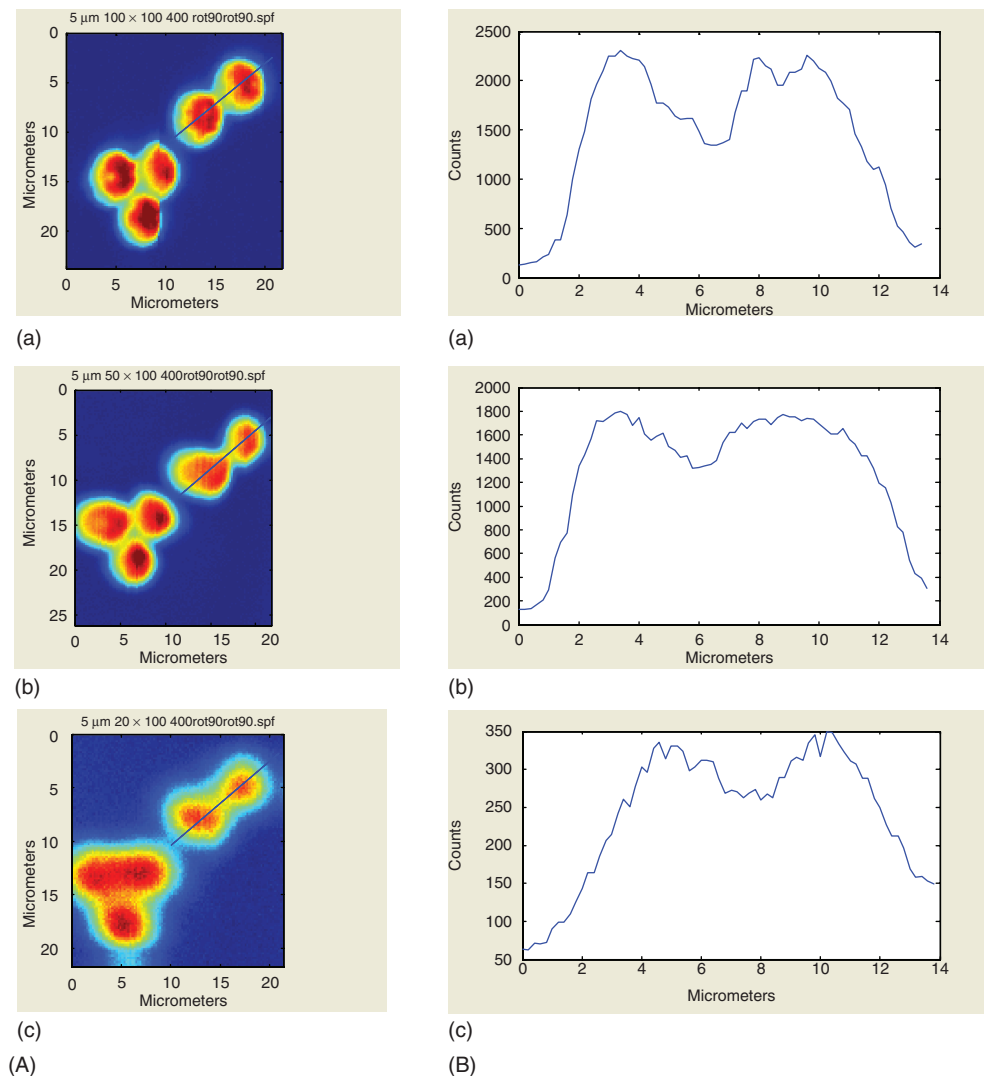
(A)

(B)

Figure 1.12 (A) Raman maps of 5.18 µm diameter polystyrene beads recorded with 100×, 50×, and 20× objectives. Increments between data points were 0.2 µm for all three images. (B) Line profiles of the two beads at the upper right. (Reproduced with permission from Ref. [38]. Copyright 2006, Avanstar Publications.)

the Raman spectra of a 20 µm thick layer of polyethylene (PE) over a 100 µm sheet of poly(ethylene terephthalate), PET. The spectra measured at different depths, including locating the focus 10 µm above the sample, are shown in Figure 1.14. It is clear that signals from the PET contribute significantly to the spectrum even when focused in or well above the PE. Everall demonstrated a similar effect when he scanned laterally across the same sample. These results were found because
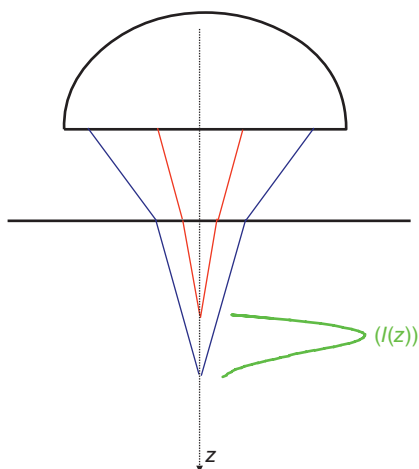
Figure 1.13 Schematic diagram showing how the effect of refraction leads to an increase in the depth of field for Raman microscopy. (Figure courtesy of Dr. Neil Everall, Measurement Science Group, Intertek Corporation.)

for every point within the entire illuminated volume of a transparent sample (not just the beam waist), there are some rays that can reach the detector. When all of these paths are added together, there can be a significant signal originating from those parts of the sample that are out of focus. This effect is particularly noticeable when the sample present in the "out-of-focus" region is a stronger Raman scatterer than the sample in the "in-focus" region. Macdonald and Vaughn have developed a simple mathematical model to quantify the contribution of "out of focus" regions of the sample [40].

1.3.4
Tip-Enhanced Raman Spectroscopy

Using the techniques discussed in the earlier sections of this chapter, it can be seen that the spatial resolution achievable by infrared or Raman microspectroscopy is governed by the diffraction limit shown in Equation 1.3. It is possible to improve on the diffraction limit in mid-infrared microspectroscopy using the techniques we describe in Chapter 12 of this book. There is also a technique, known as *tip-enhanced Raman spectroscopy* (*TERS*), whereby the spatial resolution of Raman spectroscopy can be reduced significantly below the diffraction limit [41]. TERS is a hybrid system that combines the nanometer resolution afforded by scanning probe microscopy (e.g., atomic force microscopy) with the molecular specificity of SERS. It is well known that the Raman spectrum of species with a few nanometers of roughened silver or gold surfaces is enhanced by at least four orders of magnitude. The primary enhancement in SERS arises from the electric field of the radiation being greatly increased because of resonance between the wavelength
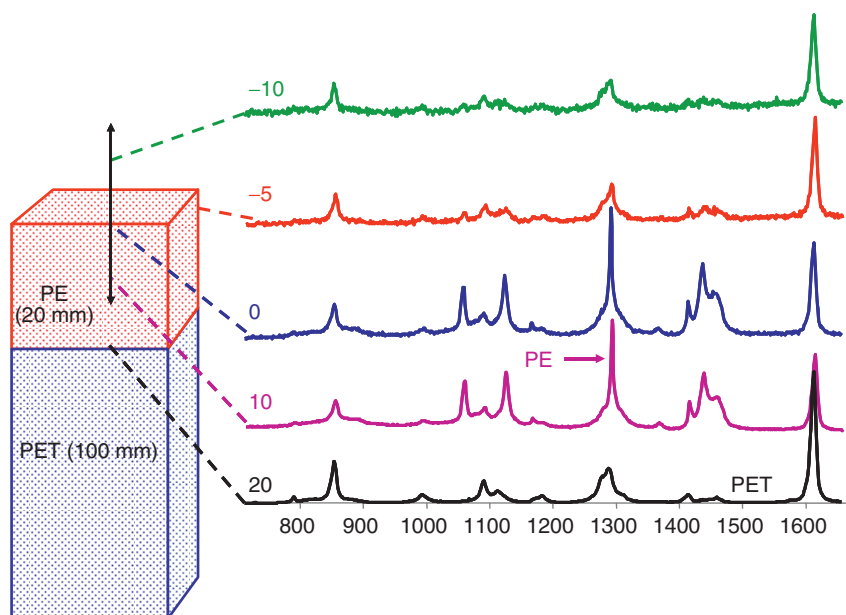
Figure 1.14 Spectra measured by raising the level of a polymer laminate sample consisting of a 100 μm layer of poly(ethylene terephthalate) under a 20 μm layer of poly(ethylene). The strongest bands in the Raman spectra of PE and PET are marked with arrows. (Figure courtesy of Dr. Neil Everall, Measurement Science Group, Intertek Corporation.)

of the illumination laser and the nearby Raman signals and the wavelengths of the surface plasmon resonance of the metal nanostructures.

It has been shown that localized plasmon polaritons in the region of sharp metal tips act in an analogous fashion, giving rise to TERS. In the usual mode of operation, TERS employs a sharp metal tip, which is illuminated from the outside to create a localized light source [42]. Alternatively, silver nanoparticles have been deposited on silica or titania surfaces and a silicon tip is used [43, 44]. TERS is rapidly becoming an important technique for microspectroscopy and is described in some detail in Chapter 11 of this book.

1.4
Near-Infrared Hyperspectral Imaging

Following the above introduction to the types of microscopes used for single-point sampling and sample mapping, the instrumentation used for hyperspectral imaging by vibrational spectrometry will now be described. NIR imaging spectrometers will be introduced first, as these are the simplest instruments in their design. Raman imaging spectrometers will then be discussed, as they bear considerable similarity to that of their NIR counterparts. The instrumentation for mid-infrared

imaging will be covered subsequently, as the principle of these instruments is somewhat different from that of NIR and Raman imaging systems. Finally, terahertz imaging that is based on a completely different principle from any of the other types of imaging instruments will be introduced.

Perhaps the simplest type of instrument for NIR hyperspectral imaging spectrometer is the one originally developed by Spectral Dimensions, Inc. (Olney, MD, USA, now Malvern Instruments). In this instrument, the radiation from a broadband source of NIR radiation (a simple tungsten or quartz–tungsten–halogen lamp) is passed through a LCTF so that a narrow region of the NIR spectrum is isolated. A typical LCTF is constructed from an interwoven stack of Lyot stages (linear polarizers and liquid–crystal variable retarders mounted on birefringent quartz crystals), usually mounted in a temperature-controlled housing. Varying the voltage applied to the liquid crystals shifts the passband in less than 1 ms without any mechanical motion or vibration of the optics. Thus, the filter can be tuned to an almost infinite number of times since there is no wear and tear.

The operation of an LCTF may be understood by considering a simplified Lyot filter stack, in which $(N + 1)$ polarizers are separated by N layers of liquid crystals sandwiched between birefringent crystals. The optical retardation, R (nm), introduced by birefringent crystals is dependent on the thickness of the crystal, d (nm), and the difference between the refractive index of the ordinary ray, n_o, and the extraordinary ray, n_e, at the wavelength of interest:

$$R = d(n_e - n_o) \tag{1.7}$$

The velocities of the extraordinary and ordinary rays differ, and they emerge from the stack with a phase delay, Γ radians, that is dependent on the wavelength λ of the radiation:

$$\Gamma = \frac{2\pi R}{\lambda} \tag{1.8}$$

The transmittance of the crystal T is given by

$$T = 0.5\cos^2\left(\frac{\Gamma}{2}\right) \tag{1.9}$$

In a typical Lyot filter, crystals are often selected so that transmission has its maximum value at the wavelength determined by the thickest crystal retarder, with other stages in the filter serving to block the transmission of unwanted wavelengths. The spectral region passed by the LCTF is dependent on the choice of polarizer, optical coating, and the liquid crystal characteristics (nematic, cholesteric, smectic, etc.). In practice, a Lyot LCTF may have as many as 11 polarizers and 10 liquid crystalline layers and is sometimes equipped with an internal microprocessor to tune all of the stages.

Wavelength scanning in NIR hyperspectral imaging spectrometers has also been accomplished with both a scanning monochromator and an acousto-optic tunable filter (AOTF). AOTFs are electro-optical devices that function as electronically tunable filters. They rely on a birefringent crystal, the optical properties of which vary upon interaction of the crystal with an acoustic wave. The resulting

compression and rarefaction of the crystal give the properties of a diffraction grating. Changes in the acoustic frequency alter the grating constant, enabling the wavelength to be tuned very rapidly. Switching time is limited only by the acoustic transit time across the crystal and is rarely greater than 50 μs. AOTFs designed for operation in the NIR region typically consist of an optically anisotropic tellurium dioxide crystal to which a piezoelectric transducer is bonded. In response to the application of an oscillating radio frequency electrical signal, the transducer generates a high-frequency acoustic wave that propagates into the crystal. The alternating ultrasonic acoustic wave induces a periodic redistribution of the refractive index through the crystal, which then acts as a transmission diffraction grating. Changing the frequency of the transducer signal applied to the crystal alters the period of the refractive index variation and, therefore, the angle through which the radiation is diffracted, and hence the wavelength band that reaches the detector. The design parameters that affect resolution include the dispersion constant of the crystalline material (related to degree of birefringence), the incidence angle, and the acousto-optic interaction length. The relative intensity of the diffracted beam is determined by the amplitude (power) of the signal applied to the crystal and by the widths of the entrance and exit slits of the monochromator.

One of the more important parameters governing which of these wavelength selection devices to use is their bandpass, that is, the full-width at half-height (FWHH) of their transmittance window. The typical bandpass of an NIR LCTF is 5 nm. As the FWHH of most bands in the NIR spectrum is greater than 10 nm, a bandpass of 5 nm is more than adequate for NIR hyperspectral imaging. The LCTF has a far higher ètendue than a monochromator operated at 5 nm resolution, although when the size of the sample being examined is very small, as it is in any microscopic measurement, the potential throughput advantage is rarely met in practice.

The bandpass of a typical AOTF ranges from several nanometers to tens of nanometers for the visible and NIR spectral regions. This resolution is suitable for fluorescence spectroscopy where bands are very broad, and is just adequate for Raman hyperspectral imaging, albeit with lower resolution than may be achieved with a monochromator. A NIR spectrometer based on an AOTF has also been sold commercially. However, the transmission of these devices for NIR hyperspectral imaging is somewhat poorer than that of LCTFs and they degrade the image quality slightly more than LCTFs. The optical efficiency of monochromators for NIR hyperspectral imaging is poorer than that of both LCTFs and AOTFs. Thus, despite the fact that the FWHH of the passband of a monochromator can be made much narrower than that of LCTFs and AOTFs, the highest performance for NIR microspectroscopy is usually found when wavelength selection is accomplished through the use of one of these devices (usually an LCTF) rather than a monochromator.

The NIR hyperspectral imaging spectrometers marketed by Malvern Instruments are equipped with a Stirling-engine-cooled indium antimonide (InSb) FPA detector with 320 pixels in one dimension and 256 pixels in the other (total 81 920

pixels) that operates in the range 1200–2450 nm. Wavelength tuning is by an LCTF with which the entire spectral range can be covered in 2 min. Alternatively, as described above, if the signal from just a few wavelengths is all that needs to be measured, the LCTF allows rapid switching between a few selected wavelengths and the measurement is over in a few seconds. A short-wavelength alternative instrument is also available that is equipped with an InGaAs FPA detector that operates in the range from 950 to 1720 nm.

As this instrument is designed for NIR operation, it is possible to use a microscope with refractive optics. In the case of the Malvern Instruments system, a refractive objective that has 1× magnification is used. With this lens, the sample is imaged directly onto the FPA detector. This objective can be easily removed and objectives with higher (micro mode) or lower (macro mode) magnification can be easily installed. Initial alignment of the sample is performed manually, but if a series of samples is to be measured, a programmable sample stage enables the sequential analysis of multiple samples.

It is probably true to say that instruments for NIR hyperspectral imaging are more versatile and rugged than corresponding instruments that measure mid-infrared and Raman spectra. However, they have two disadvantages. The first disadvantage is that the absorptivities of the overtone and combination bands in the NIR spectrum are far weaker than those of corresponding fundamentals from which they are derived. For measurements in the transmission mode, the ideal sample thickness is one that yields a low-noise spectrum with bands that are strong enough to allow rapid identification or quantification. For *mid-infrared* spectrometry, this thickness is about 10 μm. As the center wavelength of mid-infrared spectra is about 5 μm, the sample thickness is approximately equal to the smallest dimension in the $x-y$ plane that can be observed, that is, the diffraction limit when the NA is approximately equal to 0.6. For conventional NIR spectrometry (1200–2450 nm), on the other hand, the absorptivities of the stronger bands are in an order of magnitude less than the stronger fundamentals from which they are derived and so the sample thickness should be at least 100 μm. However, the diffraction-limited spatial resolution for NIR measurements is less than 3 μm if optics with an NA of 0.6 are used. Thus, even though the ultimate spatial resolution is *in principle* determined by the optics of the spectrometer, in practice this resolution is never achievable because the thickness of the sample means that the diameter of the beam waist at the top or bottom surface of the sample is larger than the diffraction-limited spatial resolution.

For short-wavelength NIR spectra (950–1720 nm), where the absorption bands are caused by transitions to the third or fourth vibrational states of C–H, N–H, and O–H stretching modes, along with weak combination bands, the situation is even worse because bands are so weak that the sample thickness must be increased to about 500 μm, even though the diffraction limit is less than 2 μm. It is at least, in part, for this reason that NIR hyperspectral imaging is rarely used for measurements with very high spatial resolution. Thus, for example, the standard

objective of the Malvern Instruments imaging spectrometer is a refractive lens with 1× magnification and low NA.

The second disadvantage of NIR hyperspectral imaging is more subtle as it is only evident for measurements of powders. Perhaps the most common application of NIR hyperspectral imaging is in the characterization of intact pharmaceutical tablets by DR spectrometry. These measurements have a significant limitation in terms of their spatial resolution caused by the effect of light scattering. Photon time-of-flight measurements [45–51] have shown that photons in diffuse transmission and reflection measurements emerge from compacted powdered samples (such as pharmaceutical tablets) in a time that is much greater than would be expected if no scattering took place. In analogous measurements made by mid-infrared DR spectrometry, Averett and Griffiths [52] estimated that the average path traveled by mid-infrared photons through very weakly absorbing samples is at least 100 particles, strongly implying that photons do not emerge from the same point into which they enter the sample. The greater the particle size, the more strongly a given particle will absorb at a given wavelength. Similarly, the greater is the scattering coefficient, the fewer particles are encountered by photons in a DR measurement and the better is the spatial resolution. For scattering samples, this effect clearly has a highly deleterious effect on spatial resolution. In DR measurements, photons are extensively scattered on entering the sample, passing through several particles (often much more than 10) before reemerging from the top surface.

The effect of scattering on spatial resolution in DR/NIR imaging was discussed by Hudak *et al.* [53] who measured the DR spectrum of polystyrene powder and then placed a clear polystyrene window of known thickness over the sample and remeasured the spectrum. From the increase in the intensity of the polystyrene bands, they were able to show that the effective path length though the powder was 1 mm ($\pm\sim$50%). The more intense the band they measured, the shorter the path length that they calculated (although these authors did not recognize the fact that the path length varied inversely with the absorptivity). They then devised a way of correlating the effective path length with the sampling volume using a random walk model to estimate the volume sampled by a typical photon (called by these authors a *voxel*). They calculated that the average path length, that is, the sampling radius from which 68% (one standard deviation) of the measured intensity imaged onto a single detector pixel originates, was between 30 and 50 µm. It is this distance, which is well over an order of magnitude greater than the diffraction limit, that determines the spatial resolution of NIR imaging measurements made in the DR mode. Since the spatial resolution of NIR hyperspectral imaging measurements of scattering samples, such as pharmaceutical tablets, is far larger than the diffraction limit, it is clear that NIR DR imaging is best used to characterize samples with a particle size that is far larger than the diffraction limit.

An alternative approach for NIR hyperspectral imaging to the one described earlier is to use a Fourier transform near-infrared (FT-NIR) spectrometer. Since the design of FT-NIR microspectrometer is more similar to that of instruments

for mid-infrared hyperspectral imaging than that of the dispersive instruments described earlier, their description will be dealt with in Section 1.6.

1.5
Raman Hyperspectral Imaging

Both Raman mapping and imaging involve the use of CCD array detectors. In mapping, the spectrum of a point of the sample is dispersed across the detector and the sample is moved after each spectrum has been measured. In Raman imaging, on the other hand, the image of the sample at a single wavelength is focused on the detector and the wavelength is changed after each measurement. Raman imaging methods can be broadly classified as line imaging or wide-field source illumination approaches [54]. In the line approach, a cylindrical lens or a Powell lens is employed to distribute the laser beam in one direction across the sample. The Powell lens is a combination of a cylindrical lens and a prism. It may be visualized as a prism with a small radius at one edge, which operates as a cylindrical lens with a radius of curvature decreasing from center to edge. The effect is a monotonic decrease in beam divergence from center to edge, so that the generated line has a nearly uniform intensity along its length [55]. The laser line dimension is oriented parallel to the direction of the entrance slit of a polychromator so that the spectrum is dispersed in the short direction of the CCD. This approach reduces the duration of the experiment by $\sqrt{n}$, where n is the number of image pixels, assuming that the laser power per pixel is kept constant. The spatial resolution parallel to the laser line is the convolution of the microscope magnification by the pixel size, whereas in the perpendicular direction it is equal to the width of the laser line convolved by the scanning precision of the instrument. As a result, the resolution in one dimension is frequently greater than in the second direction.

In wide-field or global imaging, the entire sample field-of-view is illuminated by defocusing the laser. The scattered radiation is usually first passed through a notch filter or a long-pass filter to remove the Rayleigh-scattered radiation and then through a device that blocks all but one wavelength region. This device may be a monochromator, a dichroic filter, an AOTF, or a LCTF, with the LCTF being generally favored. The wide-field approach is generally favored over line-scan imaging when high-fidelity images at a limited number of wavenumbers are desired. In wide-field imaging, the spatial resolution is determined by the convolution of diffraction, the CCD pixel size, and the microscope magnification at the focal plane of the CCD.

Surprisingly, global laser illumination leads to sample heating degradation at much lower laser intensities than point illumination because of inefficiency in conducting heat away from a surface sheet rather than a point. For steady-state measurements at a given total laser power (in watts), the optical damage threshold for a given material scales as the square root of the illuminated area (rather than linearly with the area). Thus, the laser intensity ($W\,m^{-2}$) required to damage a sample is higher for a point illumination than for line illumination, which is in

turn higher than for area illumination. There is still an advantage in distributing power over a wider area; it is just that this so-called power distribution advantage is not as great as was previously assumed [56].

As noted in Section 1.3, *confocal* microscope designs have been used in several Raman microspectrometers that allow sample mapping by moving the sample between the measurement of each spectrum. However, confocal microscopy cannot be used for wide-field Raman imaging as the entire region of the sample of interest must be illuminated and clearly the "light source pinhole" in confocal microscopes does not allow this. For hyperspectral Raman imaging, the high image quality attained by the use of confocal optics and mapping is sacrificed somewhat for data acquisition speed. However, this approach is only fast if an image is to be acquired at a single wavelength – for the acquisition of full spectra, it can be very slow.

One of the first Raman imaging spectrometers manufactured was designed and fabricated by Levin's group at the U.S. National Institutes of Health (NIH) [57]. The wavelengths for this instrument were controlled by a TeO_2 AOTF. This instrument produced high-fidelity, large-format images with a theoretical spatial resolution of about 1 μm. However, because of dispersion by the TeO_2 crystal, the finite spectral bandwidth of the AOTF resulted in a slight smearing of the output image along one axis. This degradation, which is given by the internal beam spread in the crystal, $\Delta\theta_{di}$, can be estimated from the approximate relationship reported by Suhre *et al.* [58]:

$$\frac{\Delta\theta_{di}}{\Delta\lambda} = \left(\frac{\Delta n}{n_0\lambda_0}\right)(\sin 4\theta_1 + \sin 2\theta_1)^{\frac{1}{2}} \tag{1.10}$$

where $\Delta\lambda$ is the passband (2 nm), λ_0 is the center wavelength (700 nm), Δn is the difference in refractive index of TeO_2 for the ordinary and extraordinary rays at λ_0 (0.138), n_0 is the refractive index of TeO_2 for the ordinary ray (2.177), and θ_1 is the angle between the incident beam and the optical axis of the crystal (22.5°); the values for the AOTF used by Goldstein *et al.* are given in parentheses. These values give an external beam spread, $\Delta\theta_{di}$, of 0.13 mrad (0.0037°). This value may be compared with that of the diffracted beam spread of 0.19 mrad caused by the 7 mm square aperture presented to the AOTF entrance pupil. In total, these values would lead one to predict that the image resolution along one axis would be degraded by about a factor of 2.5 on passage through the AOTF. For each AOTF passband frequency, the image on the CCD will be shifted slightly because of dispersion by the crystal, and software correction is needed if the visual and Raman images are to be correlated.

In the instrument described by Goldstein *et al.* [57], the 647.1 nm beam from a krypton ion laser was delivered to the sample by an infinity-corrected microscope objective using an epi-illumination scheme in which light from the rear housing is passed down a horizontal shaft, after which it is reflected down through the objective to the sample. The 180° backscattered light is returned to the objective and then to the spectrometer. Wavelength selection was accomplished by an AOTF that could provide either random or continuous wavelength selection.

The epi-illumination scheme preserves the linear polarization of the incident laser beam. Because the AOTF is polarization sensitive, a half-wave plate is used to rotate the plane of polarization by 180° in order to preserve the AOTF output. The collimated output from the AOTF was first imaged by a tube lens and then by a projection lens onto a liquid-nitrogen-cooled silicon CCD array. One or, occasionally, two holographic notch filters were placed in front of the detector to eliminate stray radiation from the Rayleigh line. These filters transmitted between 75% and 80% of the Raman emission beyond $75\,\text{cm}^{-1}$ of the Rayleigh line.

To minimize data acquisition time, the overall magnification of this system was made as small as possible, consistent with the spatial resolution desired. Since the image is sampled by the discrete pixels of the CCD camera, the Nyquist sampling criterion must be obeyed to avoid the generation of artifacts. There is an explicit relationship describing how the number of counts per pixel depends on the optical design. We know from Equation (1.2) that the radius of the Airy disk r is equal to $0.61\lambda/\text{NA}$ (since $x = 2r$). If the size of the CCD pixel is p, then the Nyquist sampling criterion requires that the overall magnification M satisfies the condition that $Mr > 2p$. Goldstein *et al.* designed their system such that $Mr = 2.3p$, in other words, the smallest resolvable feature was sampled by at least two pixels [57]. This rule of thumb is equally applicable to imaging spectrometers where the spatial resolution of the measurement should be spread over at least two pixels. A similar system explicitly designed for *in vivo* tissue diagnostics has been described by Vo-Dinh *et al.* [59].

ChemImage, Corp., markets a Raman imaging spectrometer that shares some of the features of the NIH instrument reported by Goldstein *et al.* but nonetheless has some significant differences. First and foremost, wavelength selection is accomplished through the use of an LCTF rather than an AOTF. The spectral bandpass of this instrument is $9\,\text{cm}^{-1}$, and it has the capability of being tuned at finer increments. It is claimed that a *spectral resolving power* of more than $0.1\,\text{cm}^{-1}$ has been consistently achieved. This term probably refers to the accuracy to which the center wavenumber of the LCTF bandpass may be set, as the FWHH of the passband of an LCTF is never as small as $0.1\,\text{cm}^{-1}$. The Raman microscope sold by Renishaw, Inc., may also be used in the imaging mode by holding the monochromator at a certain wavelength for each time increment. However, the Renishaw instruments are mainly used in the Raman microscopy and mapping modes.

1.6
Mid-Infrared Hyperspectral Imaging

1.6.1
Spectrometers Based on 2D Array Detectors

The first true mid-infrared imaging microspectrometer was reported by Levin's group at NIH and Marcott's group at Procter and Gamble [60]. They used a
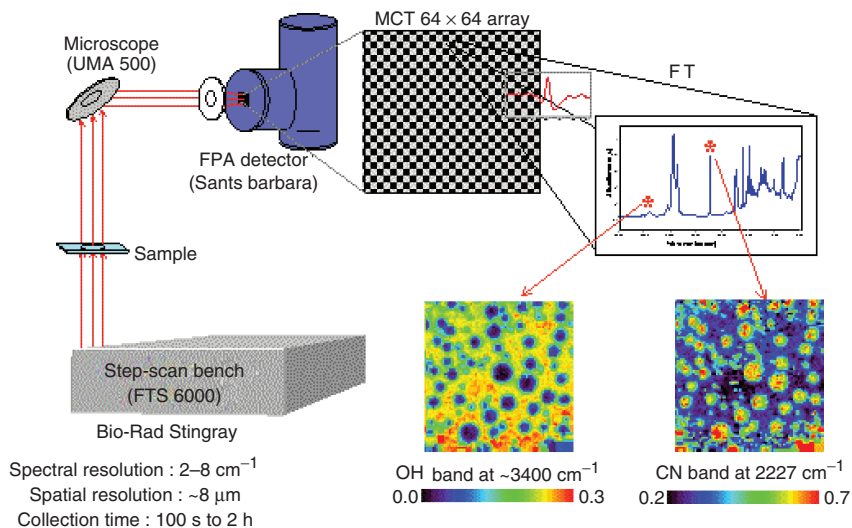
Figure 1.15 Schematic diagram of the Bio-Rad Stingray hyperspectral imaging spectrometer. (Courtesy of Agilent Corporation.)

Bio-Rad (now Agilent[2]) FTS 6000 step-scan FT-IR spectrometer equipped with a UMA-500 microscope. In their earliest instrument, the single-element detector mounted in the microscope was replaced by an indium antimonide (InSb) FPA detector with 64×64 elements imaging an average spatial area of $500 \, \mu m \times 500 \, \mu m$. A CaF_2 lens was used to focus the sample area onto the FPA detector. As InSb has a cutoff of $1800 \, cm^{-1}$, the fingerprint region of the mid-infrared spectrum could not be measured with this instrument.

A short time later, Levin's group modified their system to operate with a mid-IR MCT FPA detector. Unlike most MCT detectors used in FT-IR spectrometers, which operate in the PC mode, the pixels of MCT FPA detectors operate in the photovoltaic (PV) mode. As noted in Section 1.2.2, the cutoff wavenumber of narrow-band MCT PC detectors is at about $750 \, cm^{-1}$. The PV detector elements used in MCT FPA detectors have the same high sensitivity as narrow-band MCT PC detectors but the cutoff wavenumber is higher at about $850 \, cm^{-1}$.

The first commercial instrument employing the concepts developed by the Levin group was designed by Bio-Rad and marketed as the *Stingray* in 1995.

2) Like several other corporations in the field, the company now doing business as Varian has undergone several name changes. It was first known as Digilab, Inc. Founded in 1969, Digilab developed the first FT-IR spectrometer of the modern era, that is, the first with HeNe laser referencing, the use of a pyroelectric (TGS) detector, and the first under minicomputer control. Digilab was purchased by Bio-Rad in 1978. In 2001, Bio-Rad sold the company to a group of private investors, who renamed the company Digilab LLC. The group sold Digilab to Varian in 2004 and was later acquired by Agilent. During each of these manifestations, this organization made many of the innovations that have led to the remarkable popularity of FT-IR spectroscopy today. In this chapter, the name of the company will be given as it was when the work was reported.

This instrument is shown schematically in Figure 1.15. To maintain the image quality, a ZnSe lens was used to focus the sample image onto an MCT FPA detector rather than the Cassegrain system used in most microscopes. The instrument was equipped with a germanium long-pass filter to block visible and short-wave NIR radiation and hence to prevent detector pixel saturation and improve the SNR. A lightly sanded KRS-5 plate placed in the beam path before the condenser further improved the spatial homogeneity in the camera field-of-view and prevented the detector elements in the center of the array from saturating.

These first attempts of the mid-1990s at true mid-IR FPA imaging using a 2D MCT FPA detector were based on the detectors mounted in military heat-seeking missiles, and the spectrometers that resulted are now termed *first-generation* instruments. As the detectors used in the first-generation instruments were not designed specifically for spectroscopic imaging, they had a number of limitations. One such limitation was the tendency for pixels to "delaminate," whereby the pixels would separate from its substrate. As these first-generation detectors were designed essentially for "one use" military applications, they could not cope with the thermal stresses of repeated heating-cooling cycles from liquid nitrogen cooling.

Another major limitation arose at that time from the need to employ a step-scan interferometer. This necessity came from the relatively slow readout rates of these first-generation FPAs, which were of the order of only a few hundred Hertz. The readout rate (or *frame rate*) of an FPA detector determines the type of interferometer that must be used for FT-IR imaging, as the FPA cannot be triggered (for data transfer) any faster than its maximum readout (frame rate) speed. Since the first-generation FPAs were only capable of frame rates in the hundreds of Hertz and rapid-scanning interferometers required a faster frame rate, the use of step-scan interferometers, where the movable mirror of the interferometer could be held a given opd for several seconds, was mandated.

In 1999, Snively *et al.* [61] described the first report of the use of a rapid-scan interferometer in conjunction with a small first-generation FPA for spectroscopic imaging. In an attempt to design a mid-IR chemical imaging system designed specifically for spectroscopic applications, Digilab, together with the FPA supplier, developed and marketed the first commercial mid-infrared "rapid-scan" imaging systems in 2001, with the launch of the "second-generation" FPA, designed specifically for spectroscopic chemical imaging. These second-generation FPAs had frame rates at an order of magnitude faster than their first-generation analogs, which meant that the standard laboratory-type rapid-scanning FT-IR spectrometer could now be used for chemical imaging, significantly increasing the affordability and reducing the complexity of the system, and leading to an increase in the use and application of mid-infrared imaging spectrometers.

In addition to pioneering the developments in FPA detectors designed specifically for fast mid-infrared hyperspectral imaging, Digilab redesigned their microscope to launch the first microscope designed specifically to cater for the unique requirements of FPA-based imaging. Such improvements included a wider and

more uniform illumination FOV of up to 700 μm × 700 μm, removing the need for any diffusers, removal of refractive focusing optics, and the introduction of optical zoom capabilities to change the pixel size at the sample plane from 5.5 to 11 μm (with a corresponding increase in FOV).

The arrays used on the current generation instruments are "windowable," meaning that the area used for detection by the array can be changed. In these windowable arrays, as the window gets smaller the frame readout rate increases from several kHz for the smallest 16 × 16 windows to rates of just over 1 kHz for the largest commercially available array used in commercial instruments.

Using this windowing capability, the array can be set to a smaller dimension and the data were collected faster. Using this approach, Coutts−Lendon and Koenig [62] were able to visualize the impact of molecular weight on the dissolution behavior of a drug in aqueous systems. The overall timescale of the experiment was ~15 min with a time resolution of 15 s, providing a large enough number of data points to examine the impact of molecular weight in the system. Another characteristic of these arrays is that they are normally equipped with a Ge window that limits the spectral range from 900 to 5000 cm^{-1}. This window limits the flux on the array from NIR and visible radiation, thus allowing for longer integration times. When the window on the dewar is changed to KBr, these systems can be used in the NIR [63]. When working in this range, the visible and longer-wave infrared must be minimized. Mid-infrared radiation is attenuated by the beam splitter in the instrument and optical filters are used to remove the visible light.

The data is captured from the array in a similar manner to single-point detection. The response at each frame (all the pixels) is triggered by the interferometer as a function of opd. At each trigger, the pixel responses are readout in "snapshot" mode (i.e., all pixels are readout simultaneously), processed, and transferred to the data system to provide an interferogram data point for each pixel in the array at each opd. The triggering rate must be less than the maximum frame rate of the FPA so that all the data are collected

For a 64 × 64 FPA, the maximum frame rate is 3.77 kHz. Because of the discrete speed settings available on most commercial FT-IR spectrometers, for a spectral range of 7900 cm^{-1} (the Nyquist wavenumber for a HeNe laser-referenced system with an undersampling ratio of 2), the fastest scan speed that can currently be used to collect data from a 64 × 64 FPA is 2.5 kHz. The use of an undersampling ratio of 2 allows for data to be collected without any aliasing into the mid-IR spectral region (<4000 cm^{-1}). For a complete description of the concept of undersampling an interferogram, see Griffiths and de Haseth [64].

The interferometer speed can be increased up to 5 kHz, by further undersampling the interferogram. An undersampling ratio of 4 (where the FPA is triggered for data readout at every fourth He−Ne laser zero-crossing, that is, every second wavelength of the HeNe interferogram) provides for a Nyquist wavenumber of 3950 cm^{-1}. However, to prevent spectral artifacts caused by aliasing from appearing in the spectrum, a low-pass filter must be mounted in the optical path to prevent radiation with wavenumbers above 3950 cm^{-1} from reaching the FPA detector. These filters have benefits and drawbacks that should be considered before

use. They give the benefit of limiting detector saturation by preventing light from outside the spectral region of interest from reaching the detector, allowing longer integration times for increased SNR. However, they also reduce the intensity of the radiation in the spectral region of interest. Furthermore, in a reflection geometry experiment, there will be a double pass through the filter lowering the energy hitting the FPA.

For measurements made in this way, the FPA is still being triggered at 2.5 kHz, but now at every fourth zero-crossing. The net effect is that the interferometer speed can be increased twofold while still allowing the entire frame to be collected. At 2.5 kHz, the time available to record a frame is 0.40 ms, with typical integration times of 0.01 − 0.05 ms for high-throughput systems. In such measurements, it is clear that the FPA is typically integrating for only a fraction of the full available frame period. An unanticipated benefit of this property is that experiments with a relatively low optical throughput become more efficient.

Since the introduction of the FPA camera that is used today in various commercial instruments, there have been major changes in the array technology. Unfortunately, these changes have not been incorporated into next-generation laboratory-based imaging systems. Some of the changes that have been made include smaller pixel sizes, larger format cameras, and faster frame rates. As pointed out by Bhargava [65], all these features would benefit the spectroscopist.

The major stumbling block to the commercial use of these arrays on FT-IR instruments is their expense and US government regulations, especially the International Traffic in Arms Regulations (ITAR). These regulations govern the import and export of materials defined as defense articles, services, and technical data. The arrays that are or could be used for mid-infrared imaging are listed on the US Military Critical Technologies List (MCTL). The ITAR and the listing on the MCTL preclude sale to certain countries and require extensive paperwork for export to any other country. This constraint in itself limits sales and destroys the driver that any instrument company would have to invest in new technology and has effectively stalled the development of instruments incorporating array detectors.

By analogy with Equation 1.2, Sniveley and Koenig showed that the SNR on the baseline of spectra measured with an imaging FT-IR spectrometer is given by

$$\mathrm{SNR} = \frac{0.12\pi A\{1 - \sqrt{1 - (\mathrm{NA})^2}\}U_{\tilde{\nu}}(T)\Delta\tilde{\nu}D^*\sqrt{t}}{A_{\mathrm{D}}^{\frac{1}{2}}} \tag{1.11}$$

where NA is the numerical aperture and A is the area of the sample imaged onto the pixel. All the other parameters have the same meaning as in Equation 1.4 [66]. The factor of 0.12 is analogous to the efficiency term in Equation 1.4. Sniveley and Koenig used this equation to compare the performance of FT-IR imaging and single-detector microspectrometers and found that, for measurements near the diffraction limit, the performance of imaging spectrometers should be higher than that of standard FT-IR microspectrometers if it is assumed that the D^* of the detectors and the area of the sample imaged onto the pixel are the same in both

types of instruments. (In practice, the D^* of PV MCT detectors is slightly higher than that of PC detectors for signals modulated at frequencies greater than 1 kHz, but the difference is small.) The biggest advantage of the imaging spectrometers is in the A_D term for array detectors. Most FT-IR microscopes are equipped with 250 μm detectors, whereas the pixel size in most FPAs is 40 μm, which leads to an advantage in $\sqrt{A_D}$ by a factor of ~6 for the imaging spectrometer for measurements at close to the diffraction limit of spatial resolution.

However, the benefit in SNR of an imaging system over a single-point system when near the diffraction limit is much greater than a factor of 6. The probable reason for the significantly greater performance of the imaging spectrometers is that Equation 1.11 fails to account for the sample aperture (and its resulting degradation in étendue) when a spectrometer is operated at near the diffraction limit. Because they do not require an aperture, each entire pixel is fully illuminated in imaging systems. Consider the case of a measurement made at near the diffraction limit with a 10 μm. For a spectrometer with a single-element 250 μm detector, only 0.16% of its surface is illuminated, with the remaining 99.84% contributing only noise. When this factor is taken into account, together with the 2.5-fold improvement predicted by Equation 1.11, imaging spectrometry performed near the diffraction limit provides for SNR benefits of many orders of magnitude!

In the original design of all imaging systems, an assumption was made that the magnifications available should be those used in single-point analysis. This was the approach used by Bruker, Digilab, and PerkinElmer. As the systems were used, it became obvious that high spatial resolution was not necessary in all instances. In some cases, there were reasons for less resolution but a wider FOV since not all inhomogeneities were very small in size. The optical zoom feature mentioned above allows refractive optics to be inserted into the beam path in order to demagnify the image of the sample on the detector by a factor of two. In this way, the effective pixel size on the sample is doubled from 5.5 to 11 μm, which allows the use of very small (16 × 16) cameras. When a motorized stage is incorporated, an image can be stitched together to mimic the full image available from a 128 × 128 camera.

Other strategies have also been developed to allow for true imaging with less spatial resolution. One is the development of a 4× refractive objective. This objective provides a 1.2 mm × 1.2 mm FOV with an approximate 20 μm per pixel spatial resolution. Coupled with the optical zoom capability, larger size samples can be examined without resorting to an external compartment.

Although chemical imaging is typically performed with a microscope, it need not be limited to microscopes and samples in the micro domain. In 1998, Digilab released the "Large Sampling (LS) accessory," which consisted of an external sample compartment unit in which the FPA detector could be mounted and transferred as required between the microscope and the LS accessory. In the original design, the LS accessory could be mounted either directly off the FT-IR spectrometer or off the microscope via "pass through" optics, which allow the IR beam to bypass the internal optics of the microscope. In the current design, it is mounted on the side opposite the microscope. Under this configuration, the

overall magnification is $1:1$, so that the pixel size at the sample plane matches that of the native FPA pixel size at $40\,\mu m \times 40\,\mu m$. Therefore, with a 128×128 FPA, sample areas of up to $5.1\,mm \times 5.1\,mm$ can be imaged at once.

1.6.2
Spectrometers Based on Hybrid Linear Array Detectors

An alternative approach to hyperspectral imaging that is a hybrid of imaging and mapping was introduced in 2001 by PerkinElmer as the *Spectrum Spotlight.* This instrument is an imaging FT-IR spectrometer that incorporates a linear array of 16 narrow-band MCT PC detectors interfaced with a relatively inexpensive rapid-scanning interferometer. Though this detector is commonly (and perhaps for the sake of simplicity) often referred to as a 1×16 linear array detector, the pixels are in fact arranged in a 2×8 format. As the cutoff for the narrow-band MCT PC detectors used in this spectrometer is about $720\,cm^{-1}$, the spectral range of this instrument is at least $130\,cm^{-1}$ wider than that of the PV-MCT FPA detectors that are incorporated in most other hyperspectral imaging FT-IR spectrometers. The signals from each of the 16 detectors in the linear array are digitized simultaneously with separate ADCs. The sample is mounted on a computer-controlled stage that can be rapidly repositioned to allow the spectra from an adjacent region to be measured once the spectral data from a given stage position have been acquired. The spectra are then quilted together to produce the image. This process is repeated until the entire spatial region of interest has been covered. In addition to this linear detector array, a single $100\,\mu m$ medium-band MCT detector is mounted in the same dewar that allows individual spectra to be acquired over a wider spectral range than the spectra measured with the array. A similar instrument is now available from ThermoFisher Corporation that consists of a 28 pixel linear array arranged in a 2×14 pixel format. Other vendors have recently adopted this technology because of the lack of regulatory hurdles. It is interesting to note that these detectors are not impacted by the export control regulations that are described earlier. This is the most likely reason that this instrumentation approach has grown at the expense of the faster, higher resolution monolithic devices.

Much confusion exists as to the advantages and disadvantages of linear array versus FPA-based imaging systems, and detailed analysis and comparison is beyond the scope of this chapter. However, Bhargava and Levin proposed a useful metric to aid in comparing the performance of two imaging systems that can be conveniently applied to the comparison of a linear array system against an FPA imaging system [67]. The figure of merit defined is the pixels per minute "pixpm" and compares the performance of two imaging systems relative to each other for a specified SNR at defined spectral and spatial resolutions. The ratio of the pixpm values of two instruments is given by

$$R_{21} = \frac{n_2}{n_1} \left(\frac{t_1}{t_2} \right) \left(\frac{SNR_2}{SNR_1} \right)^2 \qquad (1.12)$$

Table 1.1 Comparison of imaging spectrometers with a 64 × 64 pixel FPA and a 16-pixel linear array.

	System 2 ($i = 2$)	System 1 ($i = 1$)
Detector	64 × 64 FPA (5.5 μm projected pixel size)	6.25 μm projected pixel size
n_i (number of pixels collected for a 700 × 700 sample area)	16 384 (four tiles)	12 544 (784 line scans)
t_i	5 min (32 scans co-added)	150 min (16 scans co-added)
SNR	200	200

where R_{21} is the ratio of the pixpm of system 2 to system 1, n_i is the number of pixels collected over the defined sample measurement area, t_i is the time required to collect image (of either one scan or to achieve the required SNR), and the SNR_i is the average SNR achieved over the sample measurement area. Hence, the relative performance is linearly related to the time and number of pixels collected and to the square of the SNR.

Let us assume the sample area to be measured is moderate in size, say 700 μm × 700 μm, and is to be collected at high spatial resolution and 4 cm^{-1} spectral resolution at an SNR of 200. Based on manufacturers' typical specifications, if all other parameters are kept equal, we have the data as shown in Table 1.1.

Thus, from Table 1.1, it can be concluded that the FPA imaging system is 30 times faster, under the specified conditions, despite requiring twice as many scans (32 vs 16). This result can be rationalized by considering the massive multichannel advantage of a 64 × 64 FPA (4096 detectors) over a 16-element linear array. There are 256 times as many detectors collecting data simultaneously for the FPA compared to that of the linear array. To cover the same 700 μm × 700 μm area, the 64 × 64 FPA, with its 5.5 μm pixel size requires a four-tile mosaic, whereas the 16-element linear array in its high spatial resolution mode of 6.25 μm requires 784 separate line scans. Thus, even though the time at which a given interferogram can be acquired with the linear array is faster than when an FPA is used, the FPA-based spectrometer required a total of 128 (4 × 32) scans, the instrument that incorporated the linear array required 12 544 (16 × 784) scans. The acquisition of almost a hundred times more scans has resulted in a significantly slower overall time of collection when the linear array is used. The smaller pixel size of the FPA system (5.5 μm) compared to that of the linear array (6.25 μm) results in more pixels being collected for the same sample measurement area, which according to Equation 1.12 further increases the advantage of the FPA-based instrument.

The differences between FPAs and linear arrays are not always of this magnitude, but they are usually in favor of the FPA-based imaging system. In fact, when employing even larger FPAs, such as the 128 × 128 FPA, the differences are even larger. Linear array systems are, however, generally at their most efficient when

operated at relatively low spatial and spectral resolutions (say 25 μm and 16 cm^{-1}, respectively) and with only a few co-added scans, where the synchronization of interferometer step and stage travel is most accurately achieved.

1.6.3
Sampling

Imaging can be accomplished using any of the approaches used in mid-infrared mapping, namely, transmission, external reflection, and attenuated total reflection. In some instruments, the microscope objective can be changed to permit operation at high or low magnification. The key to any imaging measurement is that the sample should be accurately located at a beam focus so that it can be exactly reimaged on the array detector. The first applications of mid-infrared imaging were performed in the transmission mode, with a few examples of reflection spectroscopy. Imaging by ATR took longer to be reported, even though ATR imaging is by no means a new concept. For example, in his 1967 book *Internal Reflection Spectroscopy*, Harrick showed the visible ATR image of a fingerprint recorded photographically [68].

Digilab received a patent on ATR imaging in 2000 [69]; Sommer *et al.* [70] used an ATR accessory with a germanium IRE mounted in the external beam of a *Stingray* spectrometer/microscope. They demonstrated a spatial resolution of about 8 μm in the fingerprint region and claimed to have shown that the 4× magnification factor associated with the germanium IRE was realized. However, a 4× reduction of the diffraction limit for a microscope with an NA of 0.6 should have meant that the spatial resolution was improved to 2.5 μm, and this was not explicitly demonstrated. Later Chan and Kazarian [71] reported a detailed study of ATR imaging using a patterned film of PMMA on a silicon substrate; the visible image shows circles of the polymer 4 μm in diameter with a separation of 2 μm (see Figure 1.16). Micro-ATR imaging with a diamond IRE ($n = 2.4$) showed that the PMMA circles were resolved when the spectrum was integrated between 1753 and 1672 cm^{-1} (average wavelength, $\lambda_{ave} = 5.8$ μm), but the image tended to wash out at longer wavelength as the diffraction limit was exceeded, as shown in Figure 1.17.

A detailed investigation into the resolution of ATR imaging instruments was presented by Everall [72], who first calculated the edge profile by convolving the image at 1600 cm^{-1} of the interface between the two polymers with the Airy disk, taking into account the 10 μm size of the pixels in the MCT FPA detector. He then measured the ATR image 1600 cm^{-1} of a laminate of acrylonitrile butadiene-styrene (ABS) polymer in the region of the interface using a *Stingray* imaging spectrometer equipped with a diamond ATR element. The fit was remarkably accurate, as shown in Figure 1.18.

Everall also demonstrated the problems of quantitative ATR imaging when trying to measure the image of a sample containing hard spheres with a diameter equal to or smaller than the depth of penetration [72]. He showed that shallow penetration combined with the finite spatial resolution of an imaging
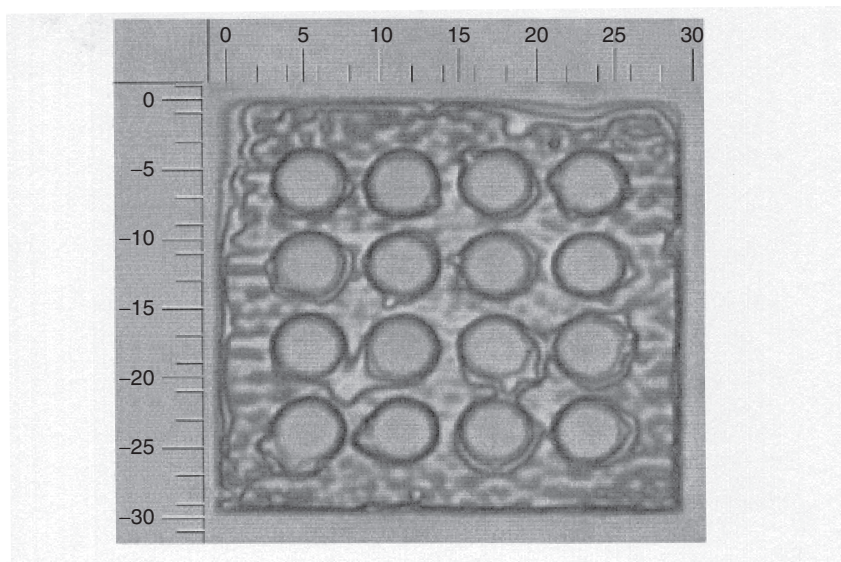
Figure 1.16 Visible image of the patterned PMMA film on a silicon wafer, captured with a 100× objective. The scales on the image are in micrometers. (Reproduced from Ref. [71]. Copyright 2003, Society for Applied Spectroscopy.)
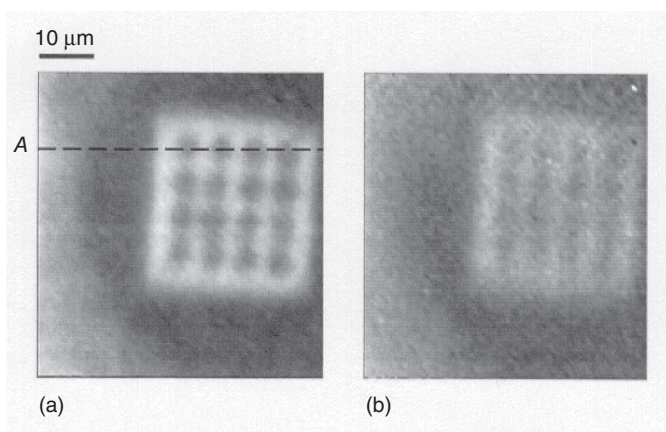

(a)   (b)

Figure 1.17 Micro-ATR images of the PMMA film on a silicon wafer obtained by integrating (a) 1753 and 1672 cm^{-1} ($\lambda_{ave} = 5.8\,\mu$m) and (b) 1179 and 1090 cm^{-1} ($\lambda_{ave} = 8.8\,\mu$m). (Reproduced from Ref. [71]. Copyright 2003, Society for Applied Spectroscopy.)

spectrometer makes ATR insensitive to hard spherical particles with domain sizes in the range $10-150\,\mu$m. For large spheres, the shallow penetration depth underestimates the diameter, whereas for small spheres, the finite spatial resolution overestimates the diameter because of blurring, causing the apparent size insensitivity of the technique for spheres. His conclusions are equally valid for
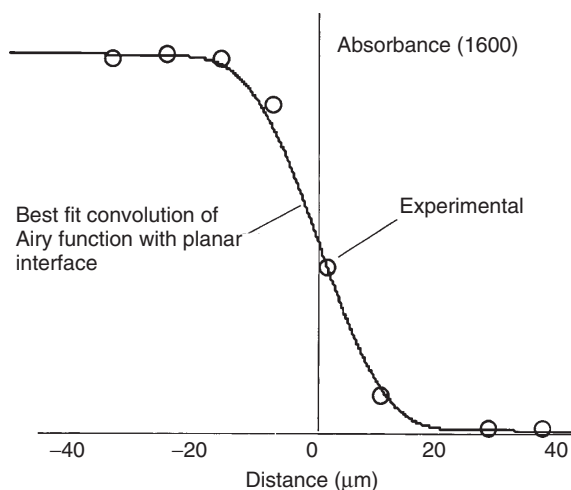
Figure 1.18 Calculated and experimental variation of the 1600 cm^{-1} band of polyurethane as a function of distance from the interface of a polyurethane–ABS laminate. (Figure courtesy of Dr. Neil Everall, Measurement Science Group, Intertek Corporation.)

other irregular inclusions, while flat or platey domains should yield more accurate results. Everall further showed that compression of soft particles increases their apparent size, albeit in a noncontrolled fashion. He stressed that ATR imaging is nonetheless a valuable technique for assessing variations in the surface composition of polymer samples. He suggested that by sectioning the samples, a more accurate picture of the near-surface composition could be obtained.

Everall's group also measured the images of polystyrene spheres of several diameters using the 1450 cm^{-1} (6.9 µm) band of polystyrene [73]. He found that transmission spectroscopy gave far better estimates of the sphere diameter than ATR imaging. The error in estimating the sphere diameter was about +10% when the diameter was 50 µm or more, whereas with ATR imaging the estimated particle diameter was considerably less than the actual diameter. When the diameter of the spheres was 10 µm or less, their apparent diameter as measured by transmission imaging was a little worse than the diffraction limit (typically about 20 µm).

To capitalize on the capability of the Agilent LS accessory, the design of the Specac "Golden Gate" single-reflection diamond accessory was modified so that it could be used in the imaging mode. Using patented optics [74], this accessory could achieve ~6.5 µm per pixel spatial resolution and could accommodate up to a 64 × 64 pixel array detector. This version of the Golden Gate optics differs from the standard version by its image-preserving optical design, which is necessary if the spatial relationships of the image are to be preserved while being propagated through the IRE. The FOV with this accessory can be as large as 640 µm × 640 µm when used with a 64 × 64 FPA detector.

Another image preserving ATR accessory that has been used in conjunction with "macro imaging" is the Harrick FastIR 75, which consists of a simple inverted

ZnSe prism such as the one shown in Figure 1.7a. Since the IRE is fabricated from ZnSe rather than diamond, this accessory is less robust, but does offer the advantage of having a considerably larger FOV. A similar accessory is made and has been used to characterize heterogeneous materials by varying the crystal and angle of incidence by Pike Technologies (Madison, WI, USA). These accessories open up a whole new avenue of research, as now one can combine the already proven and well-established benefits of ATR accessories such as limited or no sample preparation, with the information-rich content afforded by FPA chemical imaging.

In another Digilab patent [75], a "side port" adaptor directs the beam that would otherwise enter the objective (in reflection mode) via a 45° flat mirror toward the front of the instrument into an objective now facing outward. In such a configuration, the sample size is no longer limited by the working distance of the objective (typically ∼24 mm). Thus, large samples may be placed in front of the outward-facing objective for measurement. In such a configuration, only the external reflection or ATR modes of sampling are possible. This measurement mode makes it conceivably possible for large objects such as complete vehicle bumper bars to be stood on the floor and held in contact with the micro-ATR accessory on the outward-facing side port objective.

In summary, ATR imaging has a number of advantages over transmission or external reflection imaging for studying surfaces that do not have spherical or irregular inclusions, not the least of which is the absence of artifacts caused by Mie scattering. Sample preparation is much easier and the diffraction-limited spatial resolution that can be obtained is less than that could be obtained by transmission imaging by a factor equal to the refractive index of the IRE. However, because the depth of penetration is low, the peak absorbance of even quite strong bands can be rather weak, especially if a germanium or silicon IRE is used. It should also be remembered that strong bands in ATR spectra, especially those measured using IREs with a high refractive index, can be significantly shifted with respect to the same band measured in transmission mode. Finally, as noted above, if the samples contain spherical or irregular particles, they may not be adequately interrogated by the evanescent wave, making the particles appear smaller than they actually are. In an interesting example of "what goes around, comes around," Kazarian's [76] group published hyperspectral imaging data of human fingerprints in which trace quantities of drugs of abuse could be detected in a few of the spectra. The science of imaging has certainly come a long way since Harrick's original ATR photograph of a fingerprint.

1.7
Mapping with Pulsed Terahertz Radiation

Vibrational spectroscopy covers the spectral region from about 0.75 μm (∼13 500 cm^{-1}) to 1000 μm (10 cm^{-1}). To this point, we have covered the NIR (0.75−2.5 μm or ∼13 500−4000 cm^{-1}) and mid-infrared (2.5−25 μm or 4000−400 cm^{-1}) regions. The final region is the far-infrared (25−1000 μm or

$400 - 10 \, \text{cm}^{-1}$) region that is discussed in this section. Many different types of transitions are seen in the far-infrared region of the spectrum. They include intramolecular stretching modes involving heavy atoms, skeletal bending modes involving the entire molecules, torsional modes, ring-puckering vibrations of small-ring molecules, intermolecular vibrations of hydrogen−bonded molecules, and charge-transfer complexes and lattice bands (or phonon modes) [77]. Until only a few years ago, far-infrared spectra were difficult to measure and were rarely used for chemical analysis. This state of affairs was a result of the fact that the radiative energy emitted by sources of continuous far-infrared radiation, such as a Globar or high-pressure mercury lamp, is far lower than the corresponding energy emitted by mid-infrared sources. The measurement of far-infrared spectra using such sources is slow, even with a Fourier transform spectrometer.

In 2003, a completely new way of generating far-infrared radiation was developed so that far-infrared spectra can be measured faster and at higher sensitivity than before [78, 79]. As a result, there has been a renewed interest in this spectral region. To distinguish the "old way" of measuring far-infrared spectra from this "new way," this new technology has been called *terahertz spectroscopy* since the wavenumber region from 1.2 to 130 cm^{-1} corresponds to the frequency region from 0.05 to 4 THz (1 THz $= 1 \times 10^{12}$ Hz.).

The source for terahertz spectroscopy is an ultrashort-pulsed laser (usually Ti:Sapphire) that emits a stream of pulses of NIR radiation at $\sim$80 MHz, with each pulse lasting about 70 fs. The laser pulses are focused on a PC switch, sometimes known as an *Auston switch*, which is a small semiconductor crystal (often GaAs) on which two planar metal electrodes support a large electric field across its surface [80]. The design of these metal electrodes is that of an antenna. The pulses of NIR radiation cause electron−hole pairs to be generated at the surface of the semiconductor, thereby changing the conductance and effectively closing the switch. With a carefully designed antenna, the electron−hole pairs are accelerated by a DC electric field applied across the device, leading to a rapid change in the current density. The changing dipole produces a terahertz transient in the antenna that is radiated into free space. The resulting effect is the emission of short bursts of broadband coherent terahertz radiation with each laser pulse. The radiation with long wavelength that is generated by this technique can then be collected using a silicon lens.

A small fraction of the NIR laser pulse is also used in the detection process. This radiation is focused onto a second semiconductor device where, once again, electron−hole pairs are generated at the surface. On this device, however, the electric field that is created by the coincident pulses of terahertz radiation induces a measurable photocurrent. The femtosecond laser pulse effectively acts as an optical gate, which is only open for the lifetime of the electron−hole pairs in the semiconductor (<200 fs). By sweeping the time delay between the arrival of the femtosecond laser pulse and the terahertz pulse, a waveform comprising the terahertz signal as a function of time can be constructed (see Figure 1.19). The Fourier transform of this signal yields the single-beam spectrum, as shown in Figure 1.20.
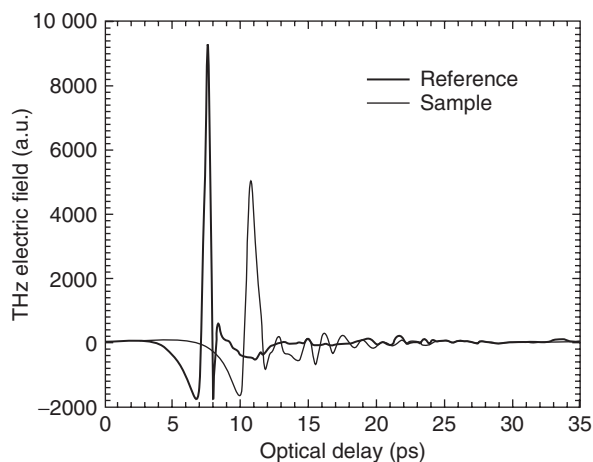
Figure 1.19 The terahertz electric field recorded as a function of time for the background(centerburst of interferogram to the left) and when the beam passes through a 4-mm thick silicon sample (centerburst of interferogram to the right).(Reproduced with permission from Ref. [78]. Copyright 2004, John Wiley and Sons, Ltd.)
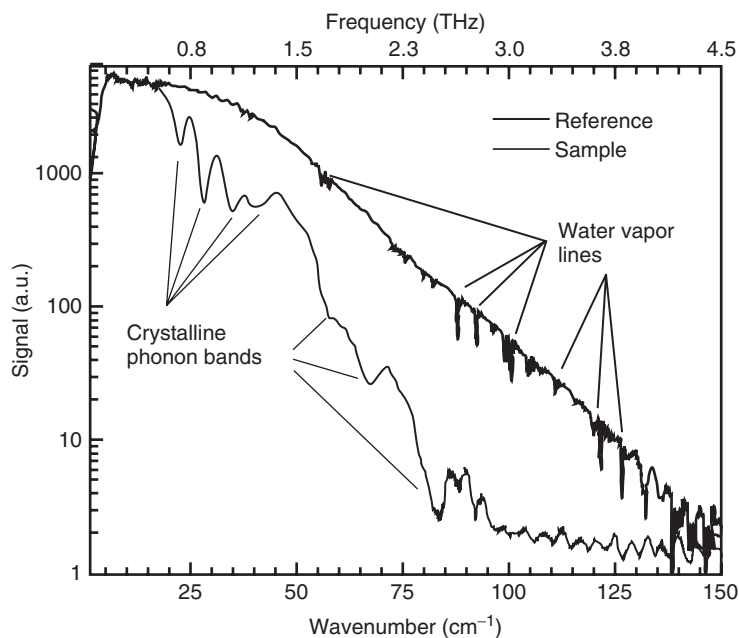

Figure 1.20 Fourier transforms of the two time domain waveforms shown in Figure 1.19. The signal is plotted on a logarithmic scale to show the dynamic range of the instrument. Pure rotation lines of water vapor are seen on the background spectrum (above). The sample spectrum (below) is that of crystalline silicon. (Reproduced with permission from Ref. [78]. Copyright 2004, John Wiley and Sons, Ltd.)
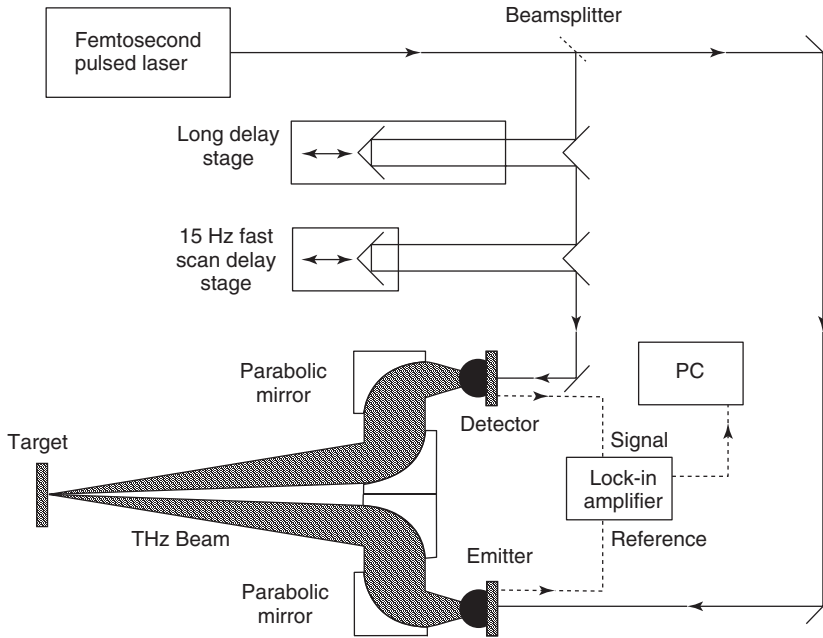
Figure 1.21 Schematic of a terahertz spectrometer. (Reproduced from Ref. [81]. Copyright 2004, John Wiley and Sons, Ltd.)

An instrument that is based on this principle, manufactured by TeraView Ltd. (Cambridge, UK), is shown in Figure 1.21 [81]. This spectrometer generates pulsed broadband terahertz radiation in the range $0.05-4\,\text{THz}$ ($1.4-130\,\text{cm}^{-1}$). Measurements made using this instrument can be recorded in two modes: a rapid-scan mode where the optical time delay is generated by mirrors that move rapidly and continuously and for which the maximum resolution is $1\,\text{cm}^{-1}$ and a step-scan mode where the time delay is generated by a cube-corner retroreflector, the position of which is controlled by a stepper motor, where the maximum resolution is $0.1\,\text{cm}^{-1}$. The rapid-scanning delay line allows both the delay position and the output of the lock-in amplifier to be digitized and re-interpolated to obtain the terahertz field as a function of optical delay in real time.

Terahertz radiation has the great advantage that, because the wavelengths are so long, scattering is minimized. Thus, it is often possible to measure a terahertz transmission spectrum through a pharmaceutical tablet or cardboard packaging material. However, the absorption spectrum of water contains a very strong broadband centered at $5.6\,\text{THz}$ ($17.9\,\text{cm}^{-1}$), which has been assigned to the resonant stretching of the hydrogen bond between the water molecules, although one of the authors of this chapter (PRG) believes that mode should be observed at a considerably higher frequency and the $5.6\,\text{THz}$ band is more likely to be due to a bending or torsional mode of the hydrogen bond. In any event, the high absorption of water in the terahertz region makes it possible to accomplish whole body imaging [82] to observe the contrast between muscle and adipose
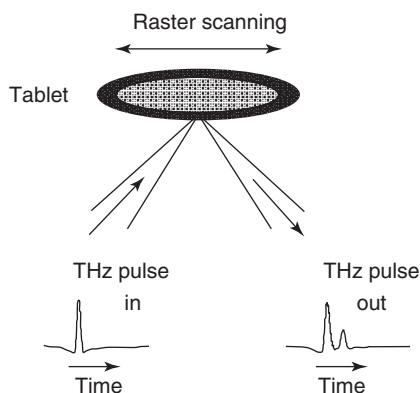
Figure 1.22 Schematic diagram of the experimental arrangement to examine the coating of a pharmaceutical tablet. (Reproduced from Ref. [85]. Copyright 2005, John Wiley & Sons, Ltd.)

tissue [83] and between tumor and normal tissue [84]. In an important related development, devices that measure images using millimeter-wave technology can now be found in most American airports.

The spatial resolution in the x and y dimensions are determined by the diffraction limit (see Equation 1.3). As λ is between ~70 and 700 µm, the resolution in these directions is far worse than for near- or mid-infrared microspectroscopy. On the other hand, significantly better resolution in the z-direction may be obtained, since the terahertz pulse duration of less than 200 fs produces an axial resolution of 30 µm. The 3D structure of the coating of pharmaceutical tablets has been studied by Fitzgerald *et al.* [85]. When the instrument is operated in the reflection mode, a reflected terahertz signal occurs whenever there is a change in boundary conditions, that is, the refractive index of two adjacent layers changes. This results in multiple pulses being returned to the detector, as shown schematically in Figure 1.22. Measurements of this type can be made in two ways. One mode allows for a rapid single-point measurement of the coating thickness. Alternatively, multipoint measurements can be made by rastering the sample to allow false color maps of the uniformity of different layers to be produced.

An example of the time domain waveforms at several points on ibuprofen tablets from two different manufacturers is shown in Figure 1.23. The lower trace is for a tablet that has a single coating, whereas the upper trace is for a tablet with multiple coatings. Knowing the refractive index of each layer, its thickness can be calculated.

1.8
Summary

Powerful instruments for mapping and hyperspectral imaging in the near-, mid-, and far-infrared regions and by Raman spectroscopy are now commercially
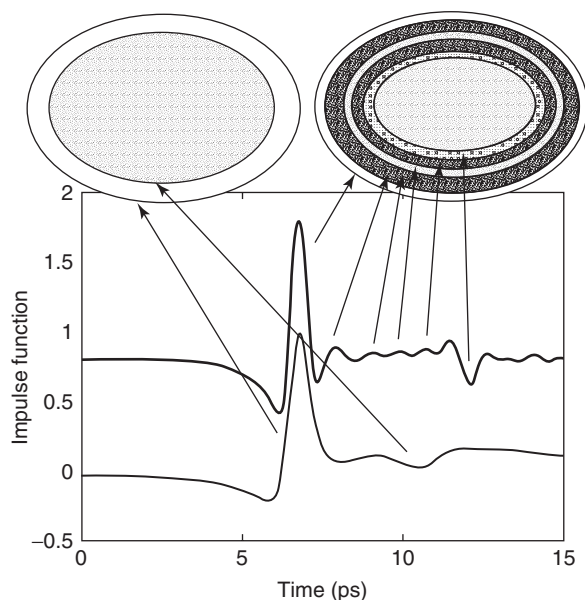
Figure 1.23 Example of depth profiling by terahertz spectroscopy. Pulses arise from interfaces between the coating layers, as illustrated by the schematic drawings of the tablets. The lower trace is for the sample on the left and the upper trace for the sample on the right. (Reproduced from Ref. [85]. Copyright 2005, John Wiley & Sons, Ltd.)

available. Though instruments for imaging were initially expensive, frequently costing more than US$200 000, the price tag is dropping. For example, with the advent of rapid-scanning FPA imaging systems, the cost of mid-infrared imaging spectrometers now starts from <US$150 000. Mapping measurements, where spectra of single points on the sample are measured sequentially and the position of the sample is changed after each measurement, are made on less expensive instruments than imaging spectrometers, but measurements are far more time consuming and spectra measured with high spatial resolution typically have decreased SNR. The hybrid linear array mapping approach, though being much faster than single-point mapping and with increased SNR and spatial resolution, is still several times less efficient in terms of speed (time), SNR, and spatial resolution than contemporary rapid-scanning FPA-based chemical imaging systems. With NIR instruments, a similar comparison cannot be made, as most imaging measurements are made by changing the wavelength with an LCTF and mapping NIR microspectrometers are rarely encountered. The situation is less definitive with Raman spectrometry, as mapping instruments are both sensitive and fast, especially with the development of EMCCDs. In summary, it can certainly be said that hyperspectral imaging spectrometers are revolutionizing the way in which vibrational spectroscopy is used, especially with respect to the analysis of pharmaceutical products and for medical diagnosis.

Acknowledgments

References

1. Burch, C.R. (1947) *Proc. Phys. Soc. London*, **59**, 41–48.
2. Barer, R., Cole, A.R.H., and Thompson, H.W. (1949) *Nature (London)*, **163**, 198–201.
3. Gore, R.C. (1949) *Science*, **110**, 710–711.
4. Blout, E.R., Bird, G.R., and Grey, D.S. (1950) *J. Opt. Soc. Am.*, **40**, 304–313.
5. Wood, D.L. (1959) *Rev. Sci. Instrum.*, **21**, 764–766.
6. Norris, K.P. (1954) *J. Sci. Instrum.*, **31**, 284–287.
7. Perkin-Elmer Instrument News, vol. 4, p. 4 (1951)
8. Rafferty, D.W. and Virnelson, R.C. (1997) *Spectroscopy*, **12** (5), 42–44.
9. Merklin, G.T. and Griffiths, P.R. (1997) *J. Chem. Phys. B*, **101**, 7408–7413.
10. Griffiths, P.R. and de Haseth, J.A. (2007) *Fourier Transform Infrared Spectrometry*, 2nd edn, Wiley-Interscience, Hoboken, NJ, pp. 277–281.
11. Griffiths, P.R. and de Haseth, J.A. (2007) *Fourier Transform Infrared Spectrometry*, 2nd edn, Wiley-Interscience, Hoboken, NJ, pp. 188–189.
12. Griffiths, P.R. and de Haseth, J.A. (2007) *Fourier Transform Infrared Spectrometry*, 2nd edn, Wiley-Interscience, Hoboken, NJ, pp. 161–168.
13. Williams, G.P. (2002) in *Handbook of Vibrational Spectroscopy*, vol. 1 (eds J.M. Chalmers and P.R. Griffiths), John Wiley & Sons, Ltd, Chichester, pp. 341–348.
14. Steiner, G., Sablinskas, V., Kitsche, M., and Salzer, R. (2006) *Anal. Chem.*, **78**, 2487–2493.
15. Griffiths, P.R. and de Haseth, J.A. (2007) *Fourier Transform Infrared Spectrometry*, 2nd edn, Wiley-Interscience, Hoboken, NJ, pp. 282–292.
16. Dumas, P. and Tobin, M.J. (2003) *Spectrosc. Eur.*, **15** (6), 17–23.
17. Levenson, E., Lerch, P., and Martin, M.C. (2006) *Infrared Phys. Technol.*, **49**, 45–52.
18. Miller, L.M. and Smith, R.J. (2005) *Vib. Spectrosc.*, **38**, 237–240.
19. Miller, L.M. and Dumas, P. (2006) *Biochim. Biophys. Acta*, **1758**, 846–857.
20. Dumas, P., Jamin, N., Teillaud, J.L., Miller, L.M., and Beccard, B. (2004) *Faraday Discuss.*, **126**, 289–302; discussion 303–311.
21. Everall, N., Lapham, J., Adar, F., Whitley, A., Lee, E., and Mamedov, S. (2007) *Appl. Spectrosc.*, **61**, 251–259.
22. Sommer, A.J. and Katon, J.E. (1991) *Appl. Spectrosc.*, **45**, 1633–1640.
23. Smith, A.L. (1958) *Appl. Spectrosc.*, **12**, 153–159.
24. Romeo, M.J., Mohlenhoff, B., and Diem, M. (2006) *Vib. Spectrosc.*, **42**, 9–14.
25. Romeo, M.J., Boydston-White, S., Matthäus, C., Miljković, M., Bird, B., Chernenko, T., Lasch, P., and Diem, M. (2008) Infrared and Raman microspectroscopic studies of individual human cells, in *Vibrational Spectroscopy for Medical Diagnosis* (eds M. Diem, P.R.

Griffiths, and J.M. Chalmers), John Wiley & Sons, Ltd, Chichester.

26. Mie, G. (1908) *Ann. Phys. (Leipzig)*, **25**, 377–452.

27. Davis, B.J., Carney, P.S., and Bhargava, R. (2010) *Anal. Chem.*, **82**, 3474–3486.

28. Davis, B.J., Carney, P.S., and Bhargava, R. (2010) *Anal. Chem.*, **82**, 3487–3499.

29. Davis, B.J., Carney, P.S., and Bhargava, R. (2011) *Anal. Chem.*, **83**, 525–532.

30. Walstra, P. (1964) *Br. J. Appl. Phys*, **15**, 1545–1552.

31. Hirschfeld, T. and Chase, B. (1986) *Appl. Spectrosc.*, **40**, 133–137.

32. Delhaye, M. and Migeon, M. (1996) *Contes Rendues Acad. Sci. Paris*, **262**, 702–705, 1513-1516.

33. Delhaye, M. and Dhamelincourt, P. (1975) *J. Raman Spectrosc.*, **3**, 33–43.

34. LaPlant, F. and Ben-Amotz, D. (1995) *Rev. Sci. Instrum.*, **66**, 3537–3544.

35. Hollricher, O. and Ibach, W. (2007) *Spectroscopy*, **2007**, 38–43.

36. Cai, T.T., Zhang, D., and Ben-Amotz, D. (2001) *Appl. Spectrosc.*, **55**, 1124–1130.

37. Savitzky, A. and Golay, M.C.E. (1964) *Anal. Chem.*, **36**, 1627–1639.

38. Adar, F., Lee, E., Mamedov, S., and Whitley, A. (2006) *Spectrosc. Suppl.: Raman*, **2006**, 38–43.

39. Everall, N.J. (2007) Paper 1820-5 at Pittcon 2007, Chicago, Illionois, February 28, 2007.

40. Macdonald, A.M. and Vaughan, A.S. (2007) *J. Raman Spectrosc.*, **38**, 584–592.

41. Pettinger, B. (2006) *Top. Appl. Phys.*, **103**, 217–240.

42. Zhang, W., Yeo, B.S., Schmid, T., and Zenobi, R. (2007) *J. Phys. Chem. C*, **111**, 1733–1738.

43. Yeo, B.S., Zhang, W., Vannier, C., and Zenobi, R. (2006) *Appl. Spectrosc.*, **60**, 1142–1147.

44. Yeo, B.S., Schmid, T., Zhang, W., and Zenobi, R. (2007) *Anal. Bioanal. Chem.*, **387**, 2655–2662.

45. Abrahamsson, C., Johansson, J., Andersson-Engels, S., Svanberg, S., and Folestad, S. (2005) *Anal. Chem.*, **77**, 1055–105.

46. Abrahamsson, C., Lowgren, A., Stromdahl, B., Svensson, T., Andersson-Engels, S., Johansson, J., and Folestad, S. (2005) *Appl. Spectrosc.*, **59**, 1381–1387.

47. Chauchard, F., Roger, J.M., Bellon-Maurel, V., Abrahamsson, C., Andersson-Engels, S., and Svanberg, S. (2005) *Appl. Spectrosc.*, **59**, 1229–1235.

48. Johansson, J., Folestad, S., Josefson, M., Sparen, A., Abrahamsson, C., Andersson-Engels, S., and Svanberg, S. (2002) *Appl. Spectrosc.*, **56**, 725–731.

49. Tsuchikawa, S. and Tsutsumi, S. (2000) *Appl. Spectrosc.*, **56**, 869–876.

50. Delphy, D.T., Cope, M., van der Zee, P., Arridge, S., Wray, S., and Wyatt, J. (1988) *Phys. Med. Biol.*, **33**, 1433–1442.

51. Long, W. and Burns, D. (1997) *Anal. Chim. Acta*, **348**, 553–563.

52. Averett, L.A. and Griffiths, P.R. (2008) *Appl. Spectrosc.*, **62**, 377–382.

53. Hudak, S.J., Haber, K., Sando, G., Kidder, L.H., and Lewis, E.N. (2007) *NIR News*, **18** (6), 68.

54. Treado, P.J. and Nelson, M.P. (2001) in *Handbook of Vibrational Spectroscopy*, vol. 2 (eds J.M. Chalmers and P.R. Griffiths), John Wiley & Sons, Ltd, Chichester, pp. 1429–1459.

55. Christensen, K.A. and Morris, M.D. (1998) *Appl. Spectrosc.*, **52**, 1145–1148.

56. Zhang, D., Hanna, J.D., Jiang, Y., and Ben-Amotz, D. (2001) *Appl. Spectrosc.*, **55**, 61–65.

57. Goldstein, S.R., Kidder, L.H., Herne, T.M., Levin, I.W., and Lewis, E.N. (1996) *J. Microsc.*, **184**, 35–45.

58. Suhre, D.R., Gottlieb, M., Taylor, L.H., and Melamed, N.T. (1992) *Opt. Eng.*, **31**, 2118–2123.

59. Vo-Dinh, T., Stokes, D.L., Wabuyele, M.B., Martin, M.E., Soon, J.M., Jafannathan, R., Michaud, E., Lee, R.J., and Pan, X. (2004) *IEEE Eng. Med. Biol. Mag.*, **2004**, 40–49.

60. Lewis, E.N., Treado, P.J., Reeder, R.C., Story, G.M., Dowrey, A.E., Marcott, C., and Levin, I.W. (1995) *Anal. Chem.*, **67**, 3377–3381.

61. Snively, C.M., Katzenberger, S., Oskarsdottir, G., and Lauterbach, J. (1999) *Opt. Lett.*, **24**, 1841–1843.

62. Coutts-Lendon, C. and Koenig, J.L. (2005) *Appl. Spectrosc.*, **58**, 976–985.

63. Miseo, E.V. and Leonardi, J. (2008) *Spectroscopy*, **2008**, 19–20.

64. Griffiths, P.R. and de Haseth, J.A. (2007) *Fourier Transform Infrared Spectrometry*, 2nd edn, Wiley-Interscience, Hoboken, NJ, pp. 63–64.

65. Bhargava, R. (2012) *Appl. Spectrosc.*, **66**, 1091–1120.

66. Snively, C.M. and Koenig, J.L. (1999) *Appl. Spectrosc.*, **53**, 170–177.

67. Bhargava, R. and Levin, I.W. (2005) in *Spectrochemical Analysis using Infrared Multichannel Detectors*, Chapter 1 (eds R. Bhargava and I.W. Levin), Blackwell Publishing Ltd, Oxford, pp. 1–24.

68. Harrick, N.J. (1967) *Internal Reflection Spectroscopy*, John Wiley & Sons, Inc., New York.

69. Burka, E.M. and Curbelo, R. (2000) *Imaging ATR spectrometer* US Patent 61,41,100 A.

70. Sommer, A.J., Tisinger, L.G., Marcott, C., and Story, G.M. (2001) *Appl. Spectrosc.*, **55**, 252–256.

71. Chan, L.A. and Kazarian, S.G. (2003) *Appl. Spectrosc.*, **53**, 381–389.

72. Everall, N.J. (2007) *Spectrometer Apparatus* Presentation on ATR Imaging at a Meeting of the Infrared and Raman Discussion Group, Sheffield, April, 2007.

73. Everall, N.J., Preistnall, I.M., Clarke, F., Jayes, L., Poulter, G., Coombs, D., and George, M.W. (2009) *Appl. Spectrosc.*, **63**, 313–320.

74. Thomson, G. and Poulter, G. (2004) *Imaging ATR spectrometer* US Patent 61,41,100 A.

75. Davis, J.R. (2003) *Infrared microscope adapter for viewing at an angle* US Patent 61,41,100 A.

76. Ricci, C., Bleay, S., and Kazarian, S.G. (2007) *Anal. Chem.*, **79**, 5771–5776.

77. Griffiths, P.R. (2001) in *Handbook of Vibrational Spectroscopy*, vol. 1 (eds J.M. Chalmers and P.R. Griffiths), John Wiley & Sons, Ltd, Chichester, pp. 229–239.

78. Taday, P.F. and Newnham, D.A. (2004) *Spectrosc. Eur.*, **16** (5), 20–24.

79. Pickwell, E. and Wallace, V.P. (2006) *J. Phys. D Appl. Phys.*, **39**, R301–R310.

80. Auston, D.H., Cheung, K.P., Valdmanis, J.A., and Kleinman, D.A. (1984) *Phys. Rev. Lett.*, **53**, 1555–1558.

81. Baker, C., Tribe, W.R., Cole, B.E., and Kemp, M.C. (2005) in *Optics and Photonics for Counterterrorism and Crime Fighting, Proceeding of the Socity Photo-Optical Instrumantion Engineering*, vol. 5616 (eds T.P. Donaldson and C. Lewis), SPIE, Bellingham, WA, pp. 61–68.

82. Siegel, P.H. (2004) *IEEE Trans. Microw. Theory Tech.*, **52**, 1538–1547.

83. Fitzgerald, A.J., Berry, E., Zinv'ev, N.N., Homer-Vanniasinkam, S., Miles, R.E., and Smith, M.A. (2003) *J. Biol. Phys.*, **129**, 123–128.

84. Pickwell, E., Fitzgerald, A.J., Cole, B.E., Pye, R.J., Ha, T., Pepper, M., and Wallace, V.P. (2005) *J. Biomed. Opt.*, **10**, 064021.

85. Fitzgerald, A.J., Cole, B.E., and Taday, P.F. (2005) *J. Pharm. Sci.*, **94**, 177–183.